REPORT DOCUMENTATION PAGE	READ INSTRUCTIONS BEFORE COMPLETING FORM

1. REPORT NUMBER ENVPREDRSCHFAC Technical Paper No. 10-74	2. GOVT ACCESSION NO.	3. RECIPIENT'S CATALOG NUMBER

4. TITLE (and Subtitle) Computation of Real-Time Currents off Southern California with Multi-Layer Hydrodynamical-Numerical Models	5. TYPE OF REPORT & PERIOD COVERED
	6. PERFORMING ORG. REPORT NUMBER

7. AUTHOR(s) T. Laevastu CAPT G. D. Hamilton, USN	8. CONTRACT OR GRANT NUMBER(s)

9. PERFORMING ORGANIZATION NAME AND ADDRESS Environmental Prediction Research Facility Naval Postgraduate School Monterey, CA 93940	10. PROGRAM ELEMENT, PROJECT, TASK AREA & WORK UNIT NUMBERS PE:63207N PN:W3713 EPRF WU 054:3-1

11. CONTROLLING OFFICE NAME AND ADDRESS Naval Air Systems Command Department of the Navy Washington, D.C. 20361	12. REPORT DATE July 1974
	13. NUMBER OF PAGES 72

14. MONITORING AGENCY NAME & ADDRESS(If different from Controlling Office)	15. SECURITY CLASS. (of this report) UNCLASSIFIED
	15a. DECLASSIFICATION/DOWNGRADING SCHEDULE

16. DISTRIBUTION STATEMENT (of this Report)

Approved for public release; Distribution unlimited.

17. DISTRIBUTION STATEMENT (of the abstract entered in Block 20, if different from Report)

18. SUPPLEMENTARY NOTES

19. KEY WORDS (Continue on reverse side if necessary and identify by block number)

20. ABSTRACT (Continue on reverse side if necessary and identify by block number)

The measurement of currents at various levels in deep water is a difficult and expensive task, and the few available measurements do not allow the construction of a coherent picture of these currents. The available general circulation models have not yet reproduced the general circulation in the desired detail and they are unable to reproduce real-time (synoptic) currents. The only method for computation of

20. (continued)

real-time currents in the ocean, including wind and tidal currents, is by the use of the Hansen type Multi-Layer Hydrodynamical-Numerical (MHN) Models.

The basic hydrodynamical formulas for the MHN model and the finite difference forms used for their solution are given in this paper. The hydrodynamical formulas used are of a linear type, with quadratic friction terms. The boundary inputs include tides at the open boundaries, wind over the whole computation area, and the initial topography of the various layer thicknesses. The currents in individual layers are vertically integrated over the thickness of the layer which is, however, variable in space and time. It is now possible to use these models with multiple open boundaries.

The results of computation of currents off Southern California with a three-layer MHN model are presented in various forms of output and some of the peculiarities of the computed currents are discussed in this paper.

Verification of the model is made by comparison with sea level changes along the coast and with available current recordings.

AB (27) The measurement of currents at various levels in deep
          water is a difficult and expensive task, and the few
          available measurements do not allow the construction of
          a coherent picture of these currents. The available
          general circulation models have not yet reproduced the
          general circulation in the desired detail and they are
          unable to reproduce real-time (synoptic) currents. The
          only method for computation of real-time currents in
          the ocean, including wind and tidal currents, is by the
          use of the Hansen type Multi-Layer
          Hydrodynamical-Numerical Models. (Modified author
          abstract)

COMPUTATION OF REAL-TIME CURRENTS OFF SOUTHERN CALIFORNIA WITH MULTI-LAYER HYDRODYNAMICAL-NUMERICAL MODELS

by

T. LAEVASTU
and
CAPT G. D. HAMILTON, USN

JULY 1974

COMPUTATION OF REAL-TIME CURRENTS
OFF SOUTHERN CALIFORNIA WITH
MULTI-LAYER HYDRODYNAMICAL-NUMERICAL MODELS

by

T. LAEVASTU and CAPT G. D. HAMILTON, USN

JULY 1974

CONTENTS

LIST OF FIGURES

Figure

LIST OF FIGURES (continued)

1. MEASUREMENT AND MODELING OF REAL-TIME CURRENTS

It is well established that ocean near-surface currents are relatively transient in character and can contain a number of large eddies (Gade, Malmberg, and Stefanson, 1965). Kvinge, Lee and Saetre (1968) found in a study of the variability of the Norwegian Sea, for example, that the basic Norwegian current can change to the opposite flow within a few days. Furthermore, they noticed drastic changes in currents related to atmospheric frontal passages. Malmberg, Gade, and Sweers (1967) found two to three day periodicities in fluctuations of both speed and direction of the permanent current flow in the area between Iceland and Greenland. Furthermore, the observations indicated a time lag between wind and surface current change of up to 24 hours. The direction of the surface current seemed at times, however, to be determined by factors other than local prevailing wind. This variability of currents is also found in areas where relatively steady currents are generally assumed to prevail, such as in the Gulf Stream regime where Defant (1940) demonstrated the great variability of currents at various levels.

It is technically difficult and expensive to make real-time current measurements in offshore areas. Furthermore the evaluation of the current recordings obtained with the recently used moored instruments pointed up considerable difficulties (e.g., swaying of the instruments in the mooring line). In any case, some reliable current recordings are presently available for offshore areas, especially in the North Atlantic Ocean. A discouraging factor in the evaluation of the available deep ocean current recordings has been the difficulty of obtaining a coherent picture of currents in space and time due to the relatively great variability over short periods of time.

Extensive efforts have been made in the last 20 years to numerically model the general circulation of the oceans. Unfortunately the models used in these attempts do not yet satisfactorily reproduce the general circulation of the oceans as we know it from the available surface current charts or from the circulation studies based on the "core"[*] method in sub-surface layers. These shortcomings are now apparent and the difficulties of reproducing the currents in the ocean with the approaches used in general circulation models has been generally recognized.

Hydrodynamical-Numerical (HN) models of the Walter Hansen type (Hansen, 1956) have been able to reproduce real-time currents in the oceans. These models have been applied in numerous cases to semi-closed shallow seas and estuaries. Lately, however, they have been applied with considerable success to deep ocean areas with multiple open boundaries by the Environmental Prediction Research Facility.

Several slightly different versions of the Multi-Layer Hydrodynamical-Numerical (MHN) models have been devised, though they have not been fully described in the available literature (see e.g., Hamilton, Williams and Laevastu (1973)). This paper describes the application of a three-layer MHN model of W. Hansen type to the relatively complex area off southern California using three open boundaries. The length of this paper does not allow exhaustive treatment of the multi-layer problem. This will be done in subsequent papers. The main objective here is to present the MHN formulas with their finite difference forms, briefly describe the treatment of the open boundaries, and show the preliminary results of the application of the model.

---

[*]The core method, developed by G. Wüst, is based on an estimation of the circulation in the ocean by following the distribution of layers of maximum salinity, oxygen minimum, or other conservative and semi-conservative properties.

2. THE BASIC MULTI-LAYER HYDRODYNAMICAL EQUATIONS AND THEIR FINITE DIFFERENCE FORMS (GIVEN FOR A THREE-LAYER MODEL)

The layer-by-layer vertically integrated hydrodynamical equations were proposed by Professor Walter Hansen (personal communication). They are analogous to the well-proven single layer HN model of the Walter Hansen type (Hansen, 1956).

$$\dot{\zeta}_1 - \dot{\zeta}_2 + H_{u1} (U1_x) + H_{v1} (V1_y) = 0 \tag{1}$$

$$\dot{\zeta}_2 - \dot{\zeta}_3 + H_{u2} (U2_x) + H_{v2} (V2_y) = 0 \tag{2}$$

$$\dot{\zeta}_3 + H_{u3} (U3_x) + H_{v3} (V3_y) = 0 \tag{3}$$

$$\dot{U}1 + \frac{r \sqrt{U1^2 + V1^2}}{H_u} U1 + fV1 + g\, \zeta_{1x} = K^{(x)} \tag{4}$$

$$\dot{U}2 + \frac{r \sqrt{U2^2 + V2^2}}{H_{u2}} U2 + fV2 + g\, \frac{\rho_1}{\rho_2}\, \zeta_{1x} + g\left(1 - \frac{\rho_1}{\rho_2}\right) \zeta_{2x} = 0 \tag{5}$$

$$\dot{U}3 + \frac{r_b \sqrt{U3^2 + V3^2}}{H_{u3}} U3 + fV3 + g\, \frac{\rho_2}{\rho_3}\, \zeta_{2x} + g\left(1 - \frac{\rho_2}{\rho_3}\right) \zeta_{3x} = 0 \tag{6}$$

$$\dot{V}1 + \frac{r \sqrt{U1^2 + V1^2}}{H_{v1}} V1 - fU1 + g\, \zeta_{1y} = K^{(y)} \tag{7}$$

$$\dot{V}2 + \frac{r \sqrt{U2^2 + V2^2}}{H_{v2}} V2 - fU2 + g\, \frac{\rho_1}{\rho_2}\, \zeta_{1y} + g\left(1 - \frac{\rho_1}{\rho_2}\right) \zeta_{2y} = 0 \tag{8}$$

$$\dot{V}3 + \frac{r_b \sqrt{U3^2 + V3^2}}{H_{v3}} V3 - fU3 + g\, \frac{\rho_2}{\rho_3}\, \zeta_{2y} + g\left(1 - \frac{\rho_2}{\rho_3}\right) \zeta_{3y} = 0 \tag{9}$$

where:

ζ_1 - surface elevation

ζ_2 - deviation of MLD (Mixed Layer Depth) from its mean (initially prescribed) depth

ζ_3 - deviation of second and third layer interface from its mean (initially prescribed) depth

U1, V1 - u,v components in first layer

U2, V2 - u,v components in second layer

U3, V3 - u,v components in third layer

r - friction coefficient (internal friction)

f - Coriolis parameter

r_b - bottom friction coefficient

g - acceleration of gravity

H - depth

ρ_1, ρ_2, ρ_3 - densities of the respective layers

$K^{(x)}$, $K^{(y)}$ - external forces

There are three interdependent continuity equations, one for each layer. These compute the change of sea level, and the change of depth, and thickness of the layers.

The equations of motion for each layer are vertically integrated through this given layer. The lower layers are driven both by internal friction and by pressure gradients.

The finite difference forms used for computation are essentially the same as in W. Hansen's single layer model, except the additional terms dictated by the presence of several layers:

$$\zeta_{(n,m,1)}^{t+\tau} = \bar{\zeta}_{(n,m,1)}^{t-\tau} - \frac{\tau}{\ell} \{ H_{u(n,m,1)}^{t} U_{(n,m,1)}^{t} - H_{u(n,m-1,1)}^{t}$$

$$U_{(n,m-1,1)}^{t} + H_{v(n-1,m,1)}^{t} V_{(n-1,m,1)}^{t} - H_{v(n,m,1)}^{t}$$

$$V_{(n,m,1)}^{t} \} - \frac{\tau}{\ell} \{ H_{u(n,m,2)}^{t} U_{(n,m,2)}^{t} - H_{u(n,m-1,2)}^{t}$$

$$U_{(n,m-1,2)}^{t} + H_{v(n-1,m,2)}^{t} V_{(n-1,m,2)}^{t} - H_{v(n,m,2)}^{t}$$

$$V_{(n,m,2)}^{t} \} \tag{10}$$

$$\zeta_{(n,m,2)}^{t+\tau} = \bar{\zeta}_{(n,m,2)}^{t-\tau} - \frac{\tau}{\ell} \{ H_{u(n,m,2)}^{t} U_{(n,m,2)}^{t} - H_{u(n,m-1,2)}^{t}$$

$$U_{(n,m-1,2)}^{t} + H_{v(n-1,m,2)}^{t} V_{(n-1,m,2}^{t} - H_{v(n,m,2)}^{t}$$

$$V_{(n,m,2)}^{t} \} - \frac{\tau}{\ell} \{ H_{u(n,m,3)}^{t} U_{(n,m,3)}^{t} - H_{u(n,m-1,3)}^{t}$$

$$U_{(n,m-1,3)}^{t} + H_{v(n-1,m,3)}^{t} V_{(n-1,m,3)}^{t} - H_{v(n,m,3)}^{t}$$

$$V_{(n,m,3)}^{t} \} \tag{11}$$

$$\zeta_{(n,m,3)}^{t+\tau} = \bar{\zeta}_{(n,m,3)}^{t-\tau} - \frac{\tau}{\ell} \{ H_{u(n,m,3)}^{t} U_{(n,m,3)}^{t} - H_{u(n,m-1,3)}^{t}$$

$$U_{(n,m-1,3)}^{t} + H_{v(n-1,m,3)}^{t} V_{(n-1,m,3)}^{t} - H_{v(n,m,3)}^{t}$$

$$V_{(n,m,3)}^{t} \} \tag{12}$$

$$U_{(n,m,1)}^{t+2\tau} = \{1-[2\tau r/H_{u(n,m,1)}^{t+2\tau}] \sqrt{\bar{U}_{(n,m,1)}^{t}{}^{2} + V_{(n,m,1)}^{*t}{}^{2}} \}$$

$$\bar{U}_{(n,m,1)}^{t} + 2\tau f V_{(n,m,1)}^{*t} - \frac{\tau g}{\ell} \{ \zeta_{(n,m+1,1)}^{t+\tau} - \zeta_{(n,m,1)}^{t+\tau} \}$$

$$+ 2\tau X_{(n,m)}^{t+2\tau} \tag{13}$$

- 11 -

$$U_{(n,m,2)}^{t+2\tau} = \{1-[2\tau r/H_{u(n,m,2)}^{t+2\tau}] \sqrt{\bar{U}_{(n,m,2)}^{t}{}^{2} + V_{(n,m,2)}^{*t}{}^{2}}\}$$

$$\bar{U}_{(n,m,2)}^{t} + 2 f\tau V_{(n,m,2)}^{*t} - \frac{\tau g}{\ell} \{\frac{\rho_1}{\rho_2} [\zeta_{(n,m+1,1)}^{t+\tau}$$

$$-\zeta_{(n,m,1)}^{t+\tau}]\} - \frac{\tau g}{\ell} \{[1-\frac{\rho_1}{\rho_2}] [\zeta_{(n,m+1,2)}^{t+\tau} -$$

$$\zeta_{(n,m,2)}^{t+\tau}]\} \qquad (14)$$

$$U_{(n,m,3)}^{t+2\tau} = \{1-[2\tau r_b/H_{u(n,m,3)}^{t+2\tau}] \sqrt{\bar{U}_{(n,m,3)}^{t}{}^{2} + V_{(n,m,3)}^{*t}{}^{2}}\}$$

$$\bar{U}_{(n,m,3)}^{t} + 2\tau f V_{(n,m,3)}^{*t} - \frac{\tau g}{\ell} \{\frac{\rho_2}{\rho_3} [\zeta_{(n,m+1,2)}^{t+\tau}$$

$$-\zeta_{(n,m,2)}^{t+\tau}]\} - \frac{\tau g}{\ell} \{[1-\frac{\rho_2}{\rho_3}] [\zeta_{(n,m+1,3)}^{t+\tau}$$

$$\zeta_{(n,m,3)}^{t+\tau}]\} \qquad (15)$$

$$V_{(n,m,1)}^{t+2\tau} = \{1-[2\tau r/H_{v(n,m,1)}^{t+2\tau}] \sqrt{\bar{V}_{(n,m,1)}^{t}{}^{2} + U_{(n,m,1)}^{*t}{}^{2}}\} \bar{V}_{(n,m,1)}^{t}$$

$$-2 \tau f U_{(n,m,1)}^{*t} - \frac{\tau g}{\ell} \{\zeta_{(n,m,1)}^{t+\tau} - \zeta_{(n+1,m,1)}^{t+\tau}$$

$$+2\tau Y_{(n,m)}^{t+2\tau} \qquad (16)$$

$$V_{(n,m,2)}^{t+2\tau} = \{1-[2\tau r/H_{v(n,m,2)}^{t+2\tau}] \sqrt{\bar{V}_{(n,m,2)}^{t}{}^{2} + U_{(n,m,2)}^{*t}{}^{2}}\} \bar{V}_{(n,m,2)}^{t}$$

$$-2 f\tau U_{(n,m,2)}^{*T} - \frac{\tau g}{\ell} \{\frac{\rho_1}{\rho_2} [\zeta_{(n,m,1)}^{t+\tau} - \zeta_{(n+1,m,1)}^{t+\tau}]\}$$

$$- \frac{\tau g}{\ell} \{[1-\frac{\rho_1}{\rho_2}] [\zeta_{(n,m,2)}^{t+\tau} - \zeta_{(n+1,m,2)}^{t+\tau}]\} \qquad (17)$$

- 12 -

$$V^{t+2\tau}_{(n,m,3)} = \{1-[2\tau r_b/H^{t+2\tau}_{v(n,m,3)}]\ \sqrt{\overline{V}^t_{(n,m,3)}{}^2 + U^{*t}_{(n,m,3)}{}^2}\}\ \overline{V}^t_{(n,m,3)}$$

$$-2\tau f\ U^{*t}_{(n,m,3)} - \frac{\tau g}{\ell}\ \{\frac{\rho_2}{\rho_3}\ [\zeta^{t+\tau}_{(n,m,2)} - \zeta^{t+\tau}_{(n+1,m,2)}]\}$$

$$- \frac{\tau g}{\ell}\ \{[1-\frac{\rho_2}{\rho_3}]\ [\zeta^{t+\tau}_{(n,m,3)} - \zeta^{t+\tau}_{(n+1,m,3)}]\} \qquad (18)$$

The computation of $\overline{U}$ and U^* is also done as in single-layer model.*

$$\overline{U}^t_{(n,m)} = \alpha U^t_{(n,m)} + \frac{1-\alpha}{4}\ \{U^t_{(n-1,m)} + U^t_{(n+1,m)}$$

$$+ U^t_{(n,m+1)} + U^t_{(n,m-1)}\} \qquad (19)$$

$$U^{*t}_{(n,m)} = \frac{1}{4}\ \{U^t_{(n,m-1)} + U^t_{(n+1,m-1)} + U^t_{(n,m)} + U^t_{(n+1,m)}\}$$

$$(20)$$

The computation of $\overline{V}$ and V^* are analogous to the corresponding U computations above. The actual depth (and thickness of the layers) is computed with the following equations:

$$H^{t+2\tau}_{u(n,m,1)} = h_{u(n,m,1)} + \frac{1}{2}\ \{\zeta^{t+\tau}_{(n,m,1)} + \zeta^{t+\tau}_{(n,m+1,1)}\}$$

$$-\frac{1}{2}\ \{\zeta^{t+\tau}_{(n,m,2)} + \zeta^{t+\tau}_{(n,m+1,2)}\} \qquad (21)$$

$$H^{t+2\tau}_{v(n,m,1)} = h_{v(n,m,1)} + \frac{1}{2}\ \{\zeta^{t+\tau}_{(n,m,1)} + \zeta^{t+\tau}_{(n+1,m,1)}\}$$

$$- \frac{1}{2}\ \{\zeta^{t+\tau}_{(n,m,2)} + \zeta^{t+\tau}_{(n+1,m,2)}\} \qquad (22)$$

---

*For the deeper layer α is substituted with α_d which has a lower value.

$$H_{u(n,m,2)}^{t+2\tau} = h_{u(n,m,2)} + \frac{1}{2} \{\zeta_{(n,m,2)}^{t+\tau} + \zeta_{(n,m+1,2)}^{t+\tau}\}$$

$$- \frac{1}{2} \{\zeta_{(n,m,3)}^{t+\iota} + \zeta_{(n,m+1,3)}^{t+\tau}\} \tag{23}$$

$$H_{v(n,m,2)}^{t+2\tau} = h_{v(n,m,2)} + \frac{1}{2} \{\zeta_{(n,m,2)}^{t+\tau} + \zeta_{(n+1,m,2)}^{t+\tau}\}$$

$$- \frac{1}{2} \{\zeta_{(n,m,3)}^{t+\tau} + \zeta_{(n+1,m,3)}^{t+\tau}\} \tag{24}$$

$$H_{u(n,m,3)}^{t+2\tau} = h_{u(n,m,3)} + \frac{1}{2} \{\zeta_{(n,m,3)}^{t+\tau} + \zeta_{(n,m+1,3)}^{t+\tau}\} \tag{25}$$

$$H_{v(n,m,3)}^{t+2\tau} = h_{v(n,m,3)} + \frac{1}{2} \{\zeta_{(n,m,3)}^{t+\tau} + \zeta_{(n+1,m,3)}^{t+\tau}\} \tag{26}$$

The following symbols were used in the finite difference formulas above:

x,y	space coordinates
t	time
U,V	components of velocity
u,v	indicators of u and v points (location) in the grid
h	initial depth (when $\zeta=0$)
ζ	surface elevation (for second and third layer it indicates the deviation of the depth of the layer from its prescribed mean value)
H	total depth ($H=h+\zeta$)
H_u, H_v	depths at u and v points respectively (also actual thickness of the layer at u and v points)
X,Y	components of external forces
$\tau^{(x)}, \tau^{(y)}$	components of wind stress

g	acceleration of gravity
f	Coriolis parameter
r	internal friction coefficient
r_b	bottom stress for lower layer
α	coefficient of horizontal eddy viscosity (also acts as a smoothing coefficient)
n,m	coordinates of the grid point, 1, 2, and 3 indicate the first (surface), second and third layer, respectively
τ	half time step
ℓ	half grid length
ρ_1, ρ_2, ρ_3	densities of first, second, and third layer

The Courant, Fredrich, Lewy stability criterion applies to the finite difference formulas given, as is the case with the single layer model.

The bottom friction coefficient used in this model (r_b) is the same as in single layer models (0.003). There are no good data available on the suitable internal friction coefficient (r) to be used. Thus numerical experiments were carried out to find a plausible value. The value of 0.0015, used in the present model gave satisfactory results.

The horizontal viscosity coefficient α (which also functions as a smoothing parameter) has the same value for the upper layers as in the single layer model (0.98 to 0.99). However, it has been found necessary to decrease this coefficient for the lower layers (0.90 to 0.92) in order to smooth out disturbances (short internal gravity waves) in the interface which occur, especially in the initial stage of the computations.

3. MODEL INPUTS AND TREATMENT OF BOUNDARIES

The three-layer model uses a staggered grid in the same manner as the single-layer HN model (Laevastu, 1972). The initial depths at u and v points were digitized from available bathymetric charts. The initial depths of the interfaces of the layers (layer thicknesses) were prescribed as horizontal "flat fields" (i.e., the same depth at each grid point). The surface elevation was also initially set to zero as is commonly done in single-layer HN models. The Southern California model (Figure 1) was set up with the geographic southern boundary (near San Diego) used as the input boundary located at the top of the grid (i.e., the grid was rotated 180°). This was done primarily for the reason that the combined tidal wave moves from the south into the area under consideration. The tidal constituents were taken from San Diego (Point Loma) tidal analyses and introduced at each time step as tidal amplitudes (Z values) along the second grid line from the top of the computational grid (the input boundary). The tidal amplitudes over deep water are usually not known. In this experimental run, the tidal amplitudes at San Diego were extended from the coast to the outer (seaward) boundary of the grid. An experiment where the tidal amplitudes over deeper water were made inversely proportional to the depth did not yield better verification than by prescribing them as equal to those in shallow water near the coast.

The internal tidal waves must also be prescribed for the input boundary at the interfaces of the selected layers. Very little is known about the internal tides. Time series measurements of temperature profiles from surface to bottom indicate that the internal tidal amplitudes are four to eight times higher than surface tides and that the amplitude relation seem to be a function of density differences between the layers.

Furthermore, there is usually a time lag in the tidal phase between surface and internal tides. In the present experimental run, the internal tide in the second layer was prescribed with a six times higher amplitude and in the third layer with a four times higher amplitude than at the surface. In addition, a two-hour time lag of phase between the layers was introduced at the input boundary.

The other open boundaries (in this case the seaward boundary and the northern boundary) must be left entirely open for inflow and outflow from the computational area. This was done by prescribing the computationally missing parameter from the next column or row inward from the boundary. Z values could be computed at both open boundaries as, for their computation, $U(n,m-1)$ and $V(n-1,m)$ were available. However, $Z(n,m+1)$ is required for computing U at the seaward boundary. Thus, the U computation do-loop stopped one grid point in from seaward boundary, and the U value at the boundary was prescribed as that of the preceding column. The U value could be computed at the lower (northern) boundary and the V could be computed at the seaward boundary. The V value can not, however, be computed at the lower (northern) boundary, because its computation requires $Z(n+1,m)$ which is not available. In this case, the V computation do-loop ends one row in from the boundary and the V value at the boundary is taken as the value one grid point up from the lower boundary. In computing $\bar{U}, U*, \bar{V}$ and $V*$ at the boundaries, the missing (outside boundary required) value (e.g., $U(n+1,m)$) was taken as the boundary value.

The permanent (thermohaline) currents can be introduced into the model by prescribing properly computed inclinations of the boundaries. This was, however, not done in the computations presented in this paper.

The wind can be prescribed at each time step at each grid point over the whole area. The computations presented here had a wind from NNW of 8 m sec^{-1}.

4. RESULTS OF THE COMPUTATION OF CURRENTS WITH A
THREE-LAYER MHN MODEL OFF SOUTHERN CALIFORNIA

The computational grid used in this work is shown in
Figure 1. The grid size was 18.532 km. This figure also
shows the locations of special points and sections A and B
from which output is presented in this paper. The harmonic
predicted tides for Long Beach and tides extracted from the
present three-layer MHN model are shown in Figure 2. Con-
sidering the relatively coarse grid used in the model, and
that the model output is taken from a point offshore (Point 3
on Figure 1) from the mareograph station, the verification
can be considered good.

Figures 3 through 26 show instantaneous portrayals of
tidal currents in the three layers at various tidal stages
which are marked in Figure 2. The features of these figures
are too numerous to describe in the text. Therefore only a
few are pointed out and the comparison of the figures are left
for readers who are interested in details of currents
(especially tidal currents) in the sea off southern California.

Figures 3 to 5 show the currents during principal low
water at Long Beach. The currents are ebbing at the surface,
but in deeper layers are changing to flooding currents and
there is, therefore, an apparent turning of currents to the
left relative to the surface current. (Note the change of
speed scales between the surface and deeper layer current
plots.) The currents in the second and third layers are
relatively similar in direction, but bottom currents (third
layer) are weaker than the currents in the second layer.

Figures 6 to 8 show the currents two hours after principal
low water at Long Beach. The relation of currents between the
different layers is more complex than two hours earlier. There
is a noticeable convergence in the central area in the second
layer, whereas currents are flooding fully in the third layer.

Figures 9 to 11 show currents at secondary high water at Long Beach. Flooding currents occur in all layers. The currents in the deeper layers turn towards the right with relation to surface layer currents.

Figures 12 to 14 show currents two hours later when the current is changing to ebb in all layers.

Figures 15 to 17 show the currents during secondary low water at Long Beach. The currents are ebbing in the surface layer and are turning to flood currents in the lower layer, with an apparent turn to the left. However, the currents in the third layer turn somewhat to the right as compared to the second layer.

Figures 18 to 20 give the currents two hours later. The currents are still ebbing at the surface but are starting to flood in the lower layers. The currents in the deeper layer now run to the right in relation to the surface layer.

Figures 21 to 23 show the currents during principal high water at Long Beach. There are still ebbing currents at the surface but flooding in deeper layers. The currents two hours later (Figures 24 to 26) show the same condition, except the deep layer currents now turn more consistently to the right with relation to the surface layer.

Figures 27 to 36 show the tidal curves, the change of the depth of interfaces between the second and third layers, and currents and current roses at special output points. The locations of these output points are given in Figure 1. There are considerable differences in the behavior of currents from one location to another as could be expected by the special bathymetric features.

Figure 37 gives the depth along sections A and B (see Figure 1 for locations) and the Figures 38 to 41 show the change of the depth of the interfaces.

Figures 42 to 45 show the sea level topography at the four special output times (see Figure 2) and Figures 46 to 49 show the topography of the bottom of the first layer (the Mixed Layer Depth). Greatest changes in the MLD occur at the continental slope (as also known from empirical observations).

Figure 50 shows the rest currents (residual current after a full tidal cycle) with a NNW wind of 8 m sec^{-1}. As seen, the rest current is largely determined by the prescribed prevailing wind.

No coherent data on the tidal current regime off southern California are available from empirical measurements as such measurements have not been carried out systematically in this area. However, some attempts have been made by Jones (1971) to construct the average geostrophic surface flow in the area under consideration. Some similarities between the current features presented here and that of the circulation picture presented by Jones can be recognized.

5. SUMMARY

The hydrodynamical formulas and their finite difference forms for a 3-layer MHN model of W. Hansen type given in this paper present a model for which the properties are vertically integrated through any given layer. Reliable information on the proper value of the internal friction coefficient does not exist and an experimental value was used in the program.

The computational results reveal the following points:

(1) A comparison of harmonic predicted tides and tides extracted from the MHN model are in good agreement despite a coarse grid (18.532 km) and extrapolation of coastal tidal harmonic constituents outward to the open boundary.

(2) The currents in deeper layers turn, in most cases, toward the right of the current direction in the surface layer. However, occasional left turns can be noticed in changing regimes (i.e., when tidal currents in coastal areas change from ebb to flood).

(3) The interface between the layers deepens off the continental slope and the largest fluctuations are also shown by the model in this region. This behavior of the MLD is in agreement with observations as the greatest MLD fluctuations (internal waves) are usually observed at the continental slope.

(4) The model shows a time lag in the time of low (or high) water in different layers. This time lag varies with location.

(5) The general conclusion from this paper is that the real-time currents, including tidal currents can be reproduced with Multi-Layer Hydrodynamical-Numerical models with multiple open boundaries, provided that correct input boundary conditions can be prescribed.

REFERENCES

Defant, A., 1940: Die Lage des Forschungsschiffes "Altair"
      auf der Ankerstation, 16 bis 20. Juni 1938 und das auf
      ihr gewonnene Beobachtungsmaterial. <u>Okt. Beih. Ann.</u>
      <u>Hydrogr. Marit. Met</u>. 355 pp.

Defant, A., 1940: Die ozeanographischen Verhältnisse während
      der Ankerstation des "Altair" an Nordrand des
      Hauptstromstriches des Golfstromes nördlich der Azoren.
      <u>Nov. Beih, Ann Hydrogr. Marif. Met</u>. 355 pp.

Gade, H.G., S.A. Malmberg and U. Stefansson, 1965: Report
      on the joint Icelandic-Norwegian expedition to the area
      between Iceland and Greenland 1963. <u>NATO Subcom. Oceanogr.</u>
      <u>Techn. Rpt. 22</u>.

Hamilton, G.D., F.R. Williams and T. Laevastu, 1973: Computa-
      tion of tides and currents with Multi-layer Hydrodynamical
      Numerical (MHN) models with several open boundaries.
      <u>Proc. 1973 Summer Simulation Conference, 634-649</u>.

Hansen, W., 1956: Theorie zur Errechnung des Wasserstandes und
      der Strömungen in Randmeeren nebst Anwendungen. <u>Tellus</u>
      8: 287-300.

Jones, J.H., 1971: General circulation and water character-
      istics in the Southern California Bight. <u>So. Cal. Coast.</u>
      Water Res. Proj., Publ. 37 pp.

Kvinge, T., A. Lee and R. Saetre, 1968: Report on study of
      variability in the Norwegian Sea April/May 1967, Rpt.
      <u>Geophys. Inst. Univ. Bergen</u>. (Mimeo)

Malmberg, S.A., H.G. Gade and H.E. Sweers, 1967: Report on
      the second joint Icelandic-Norwegian expedition to the
      area between Iceland and Greenland in August-September,
      1965. <u>NATO Subcom. Oceanogr. Techn. Rpt. 41</u>.
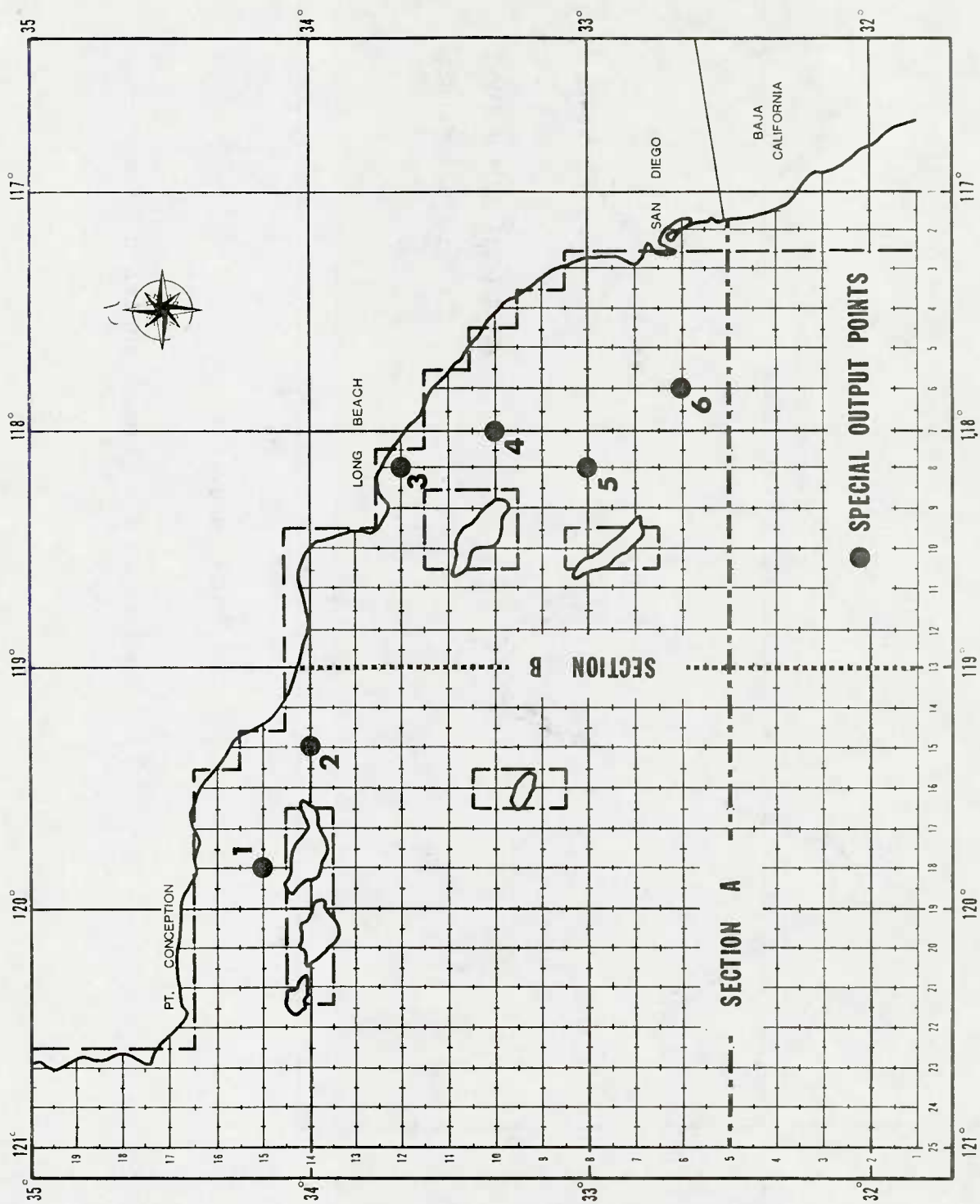
Figure 1. The computational grid and locations of special output points and sections.
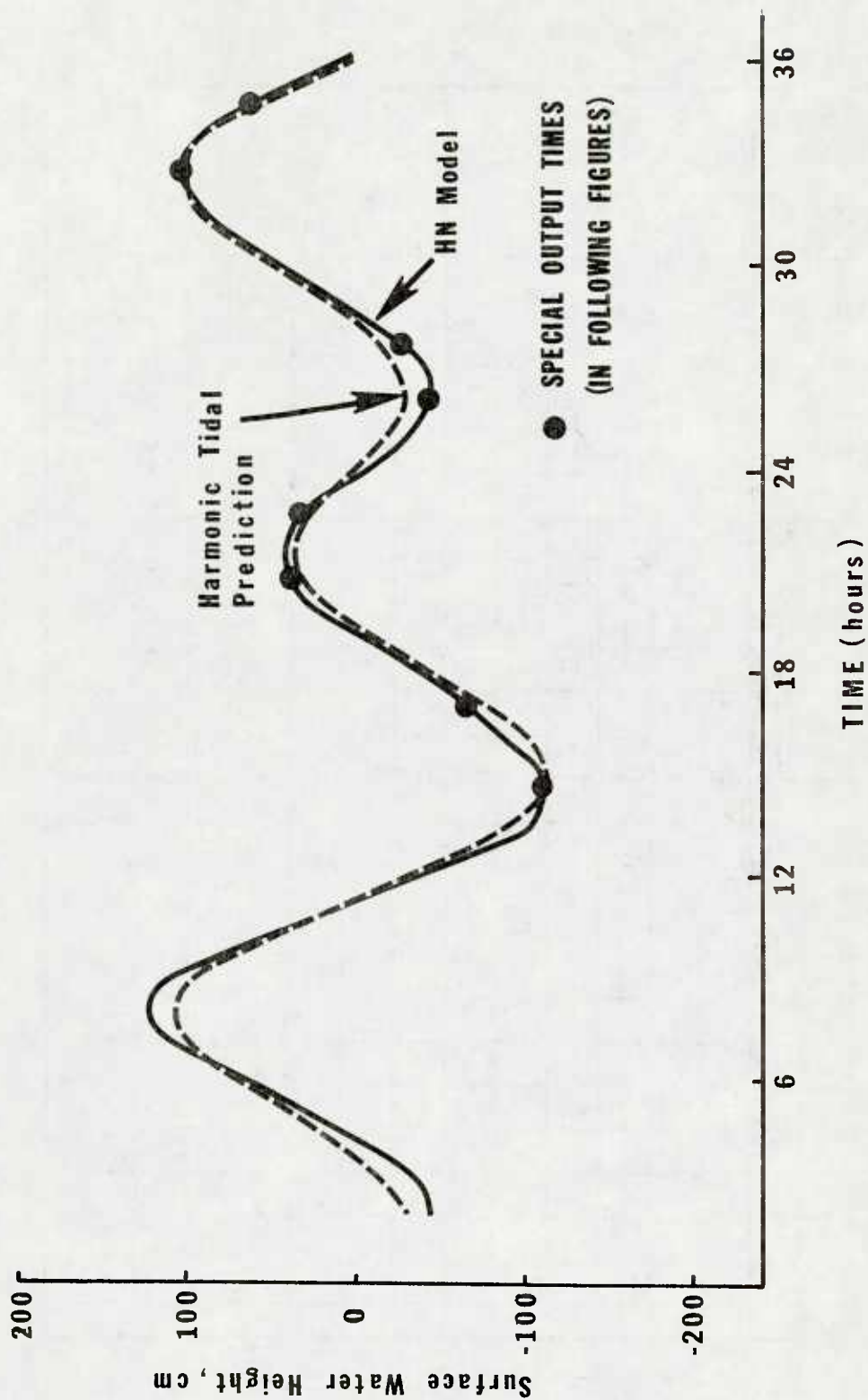
Figure 2. Tides at Long Beach, computed with HN model and with harmonic tidal prediction model (special output times are also shown on this figure).
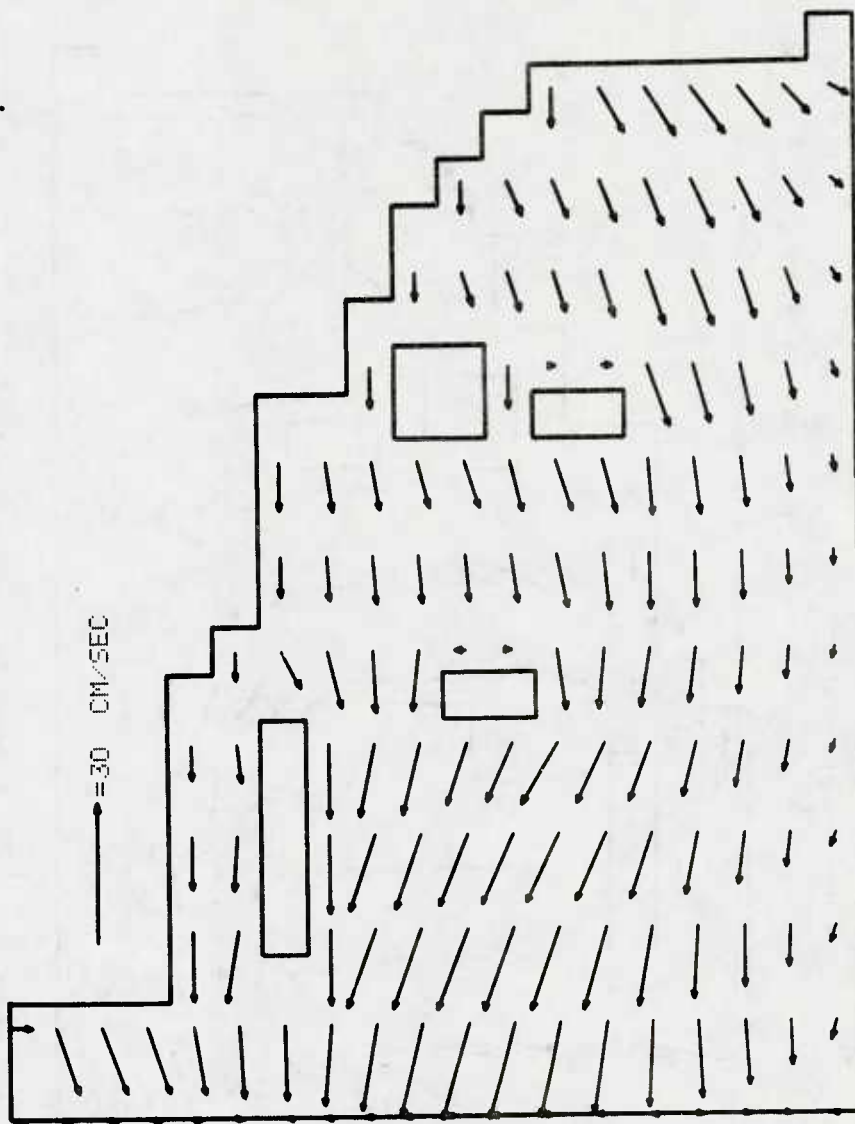
Figure 3. Currents in the surface layer during principal low water at Long Beach.

=30 CM/SEC
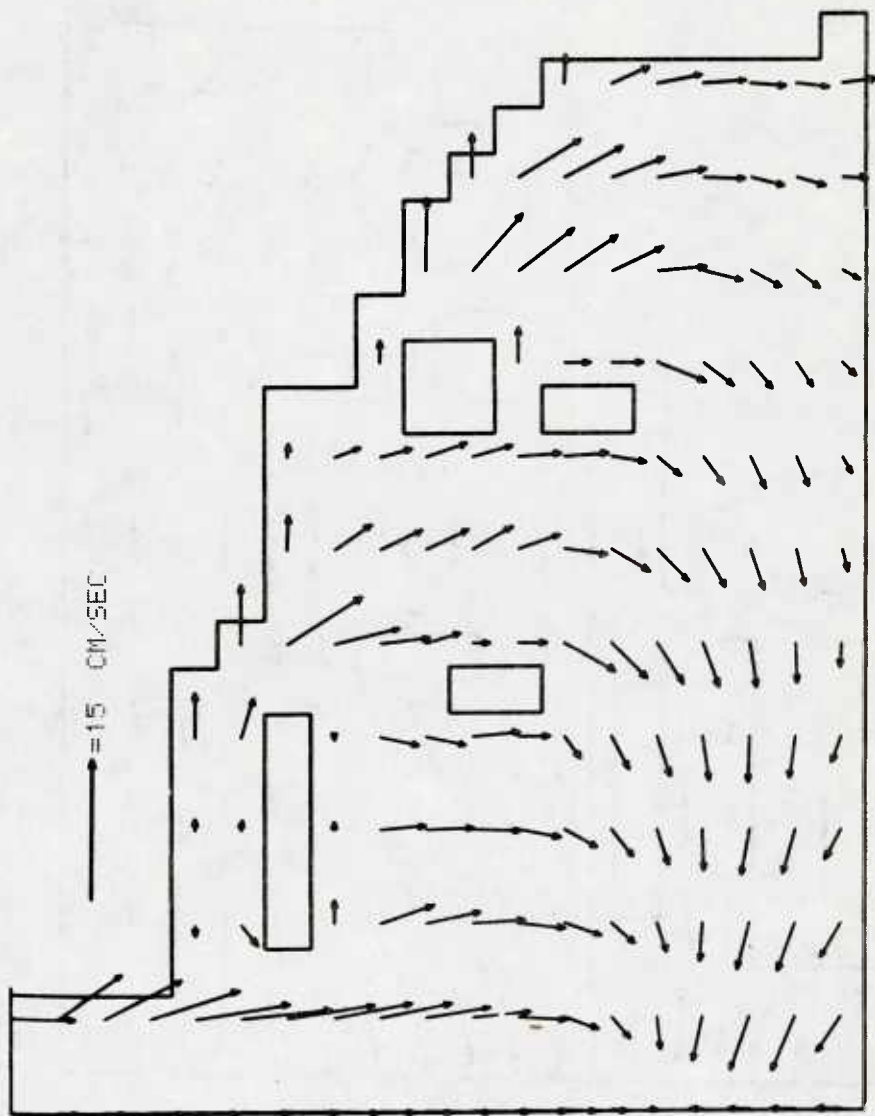
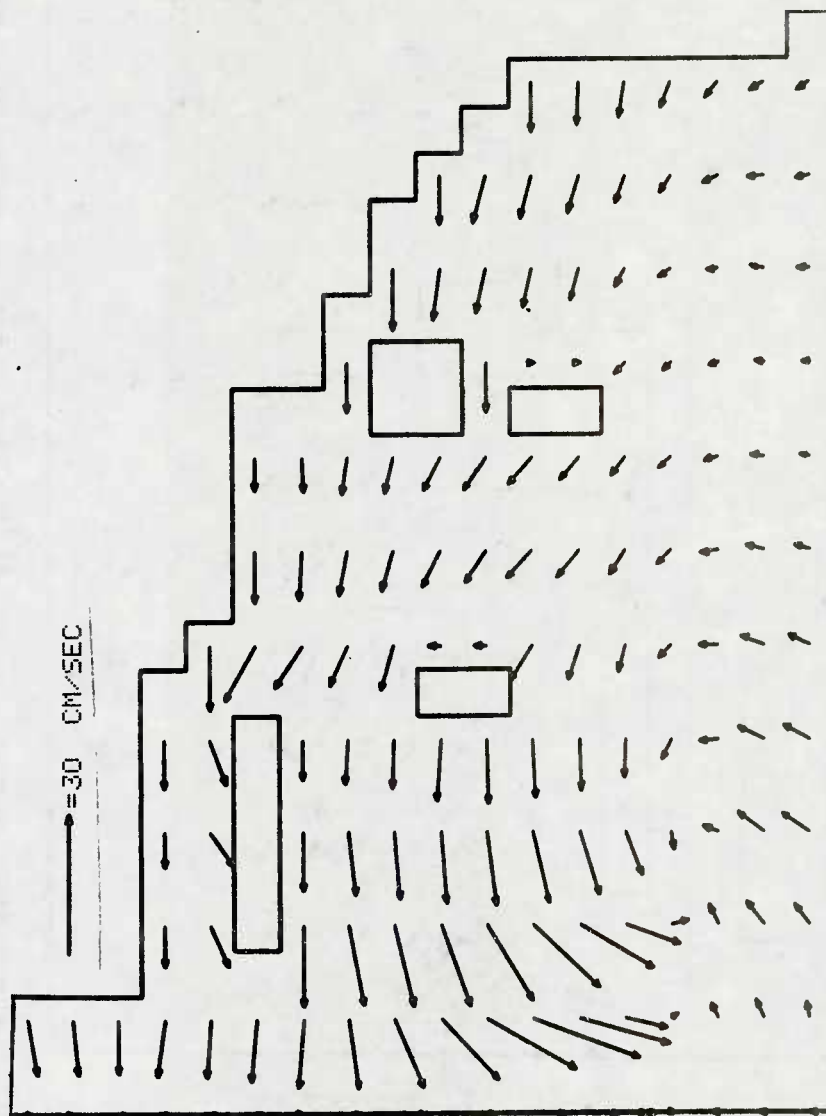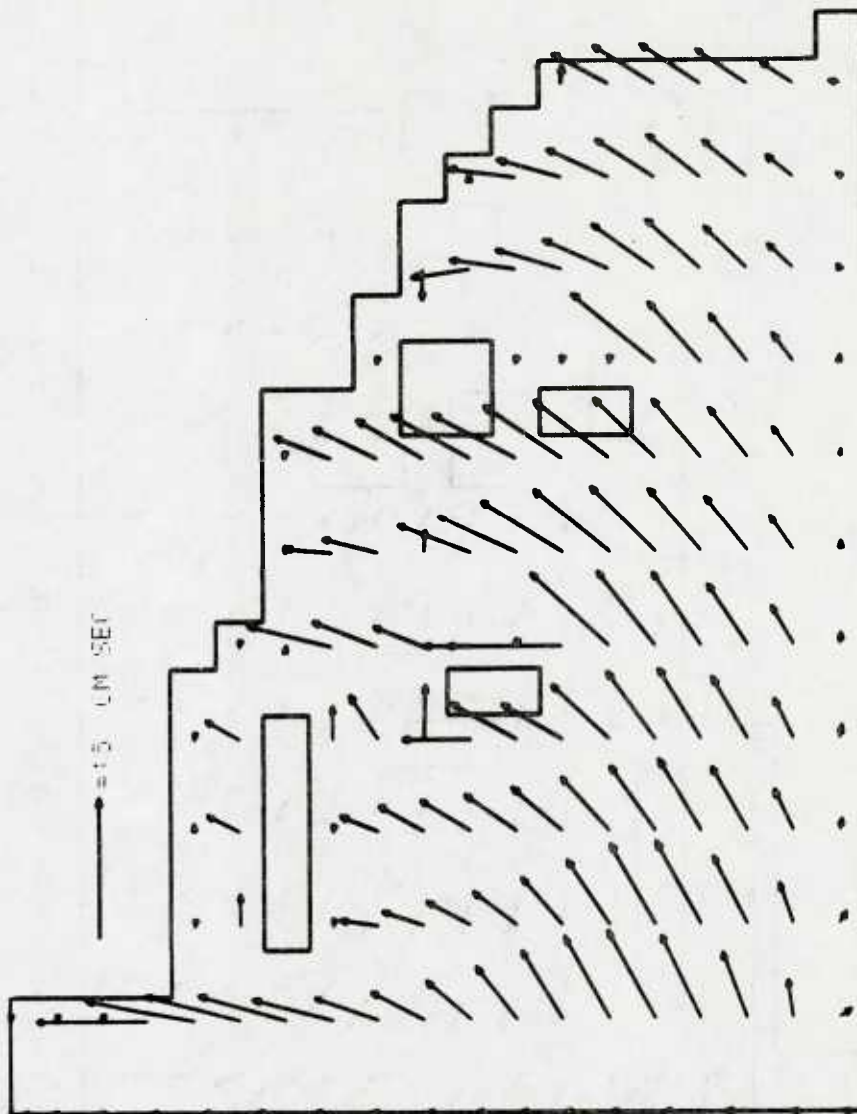Figure 4. Currents in the intermediate layer during principal low water at Long Beach (note the change of speed scale with respect to Figure 3).
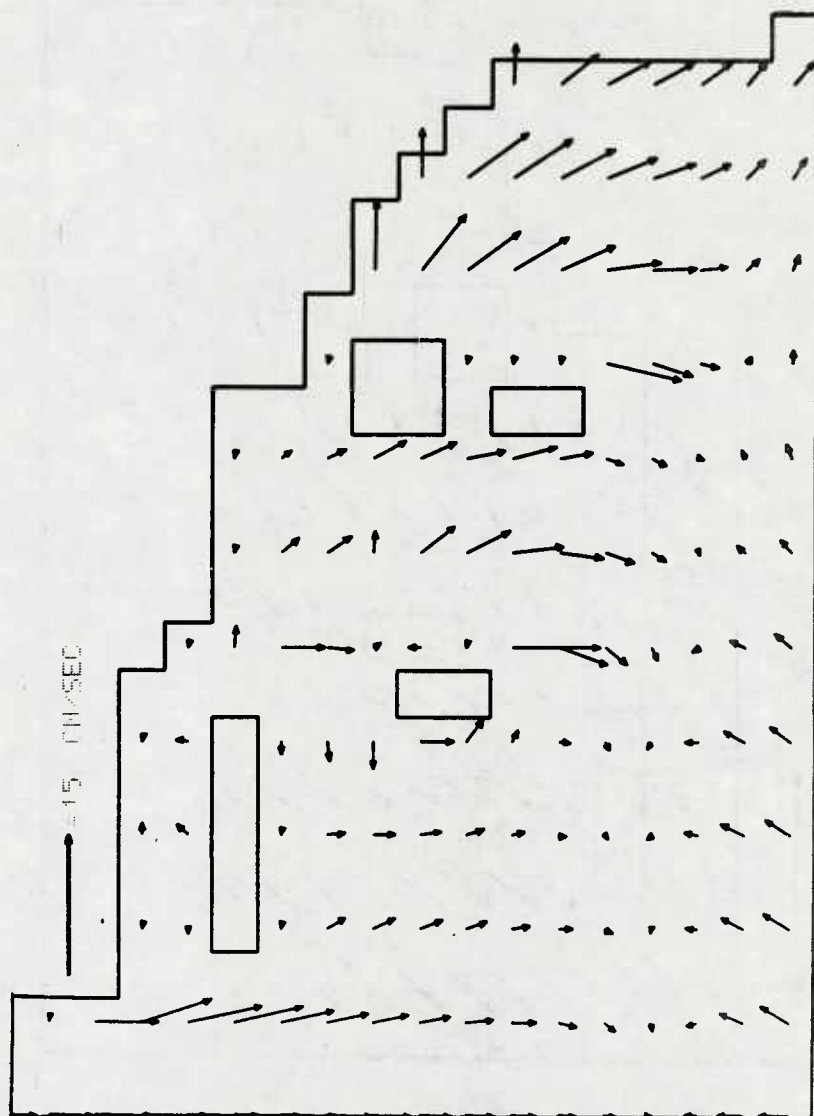
Figure 5. Currents in the bottom layer during principal low water at Long Beach.
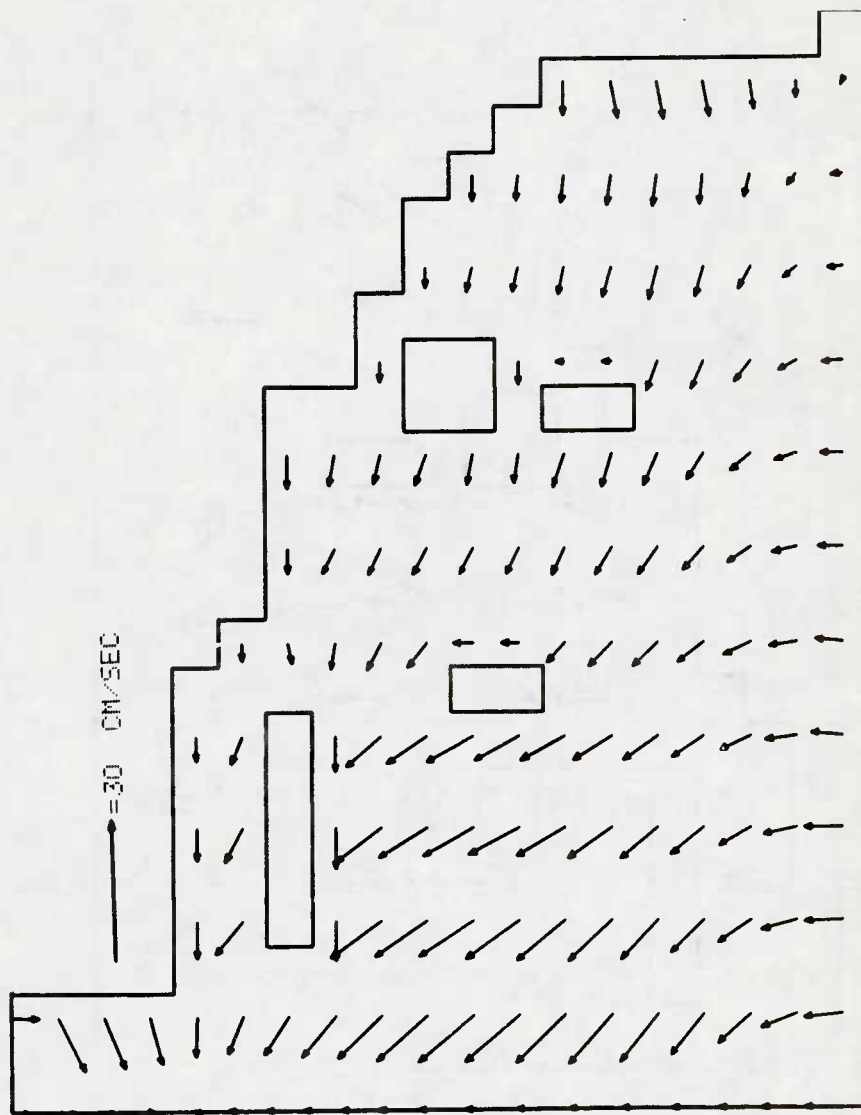
Figure 6. Currents in the surface layer 2 hours after principal low water at Long Beach.

=30 CM/SEC
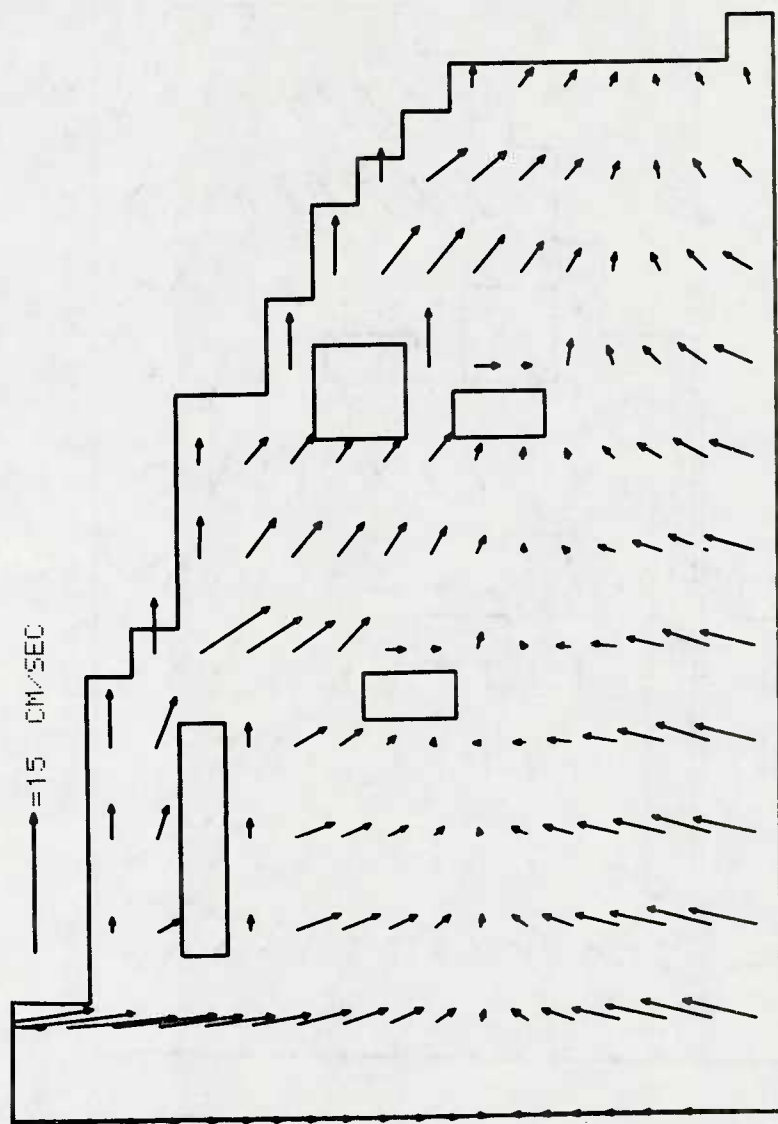
Figure 7. Currents in the intermediate layer 2 hours after principal low water at Long Beach.

=15 CM/SEC
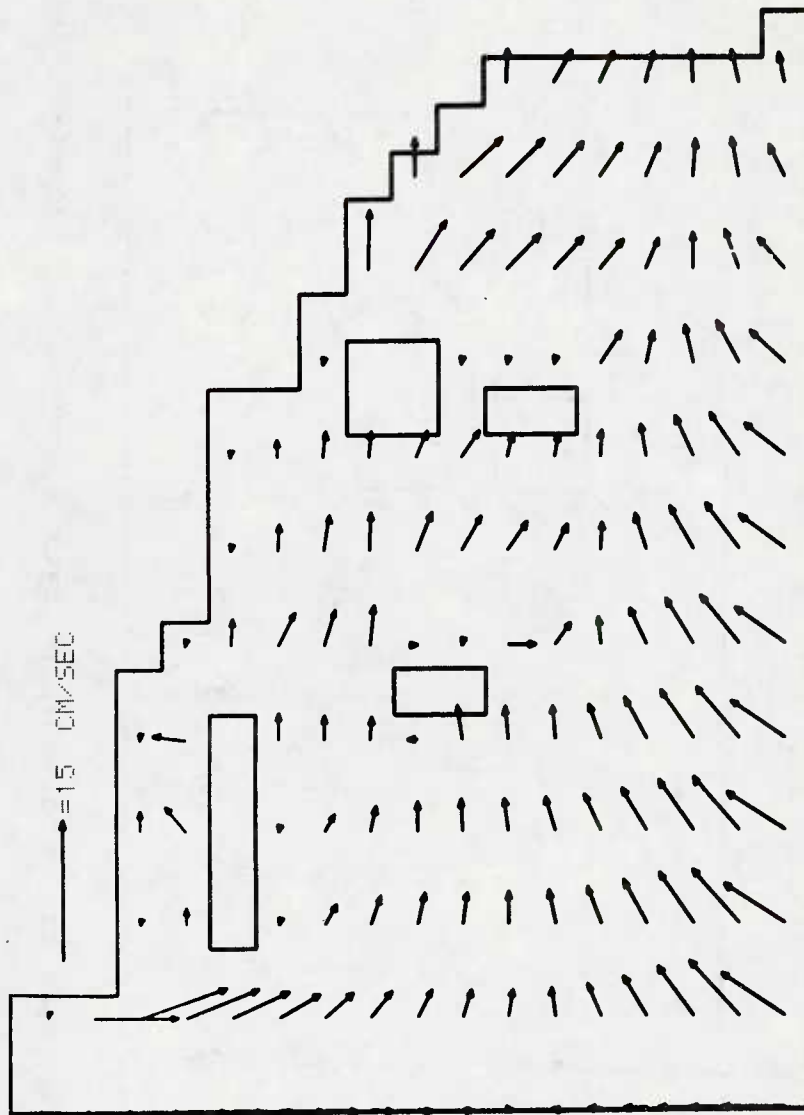
Figure 8. Currents in the bottom layer 2 hours after principal low water at Long Beach.

=15 CM/SEC
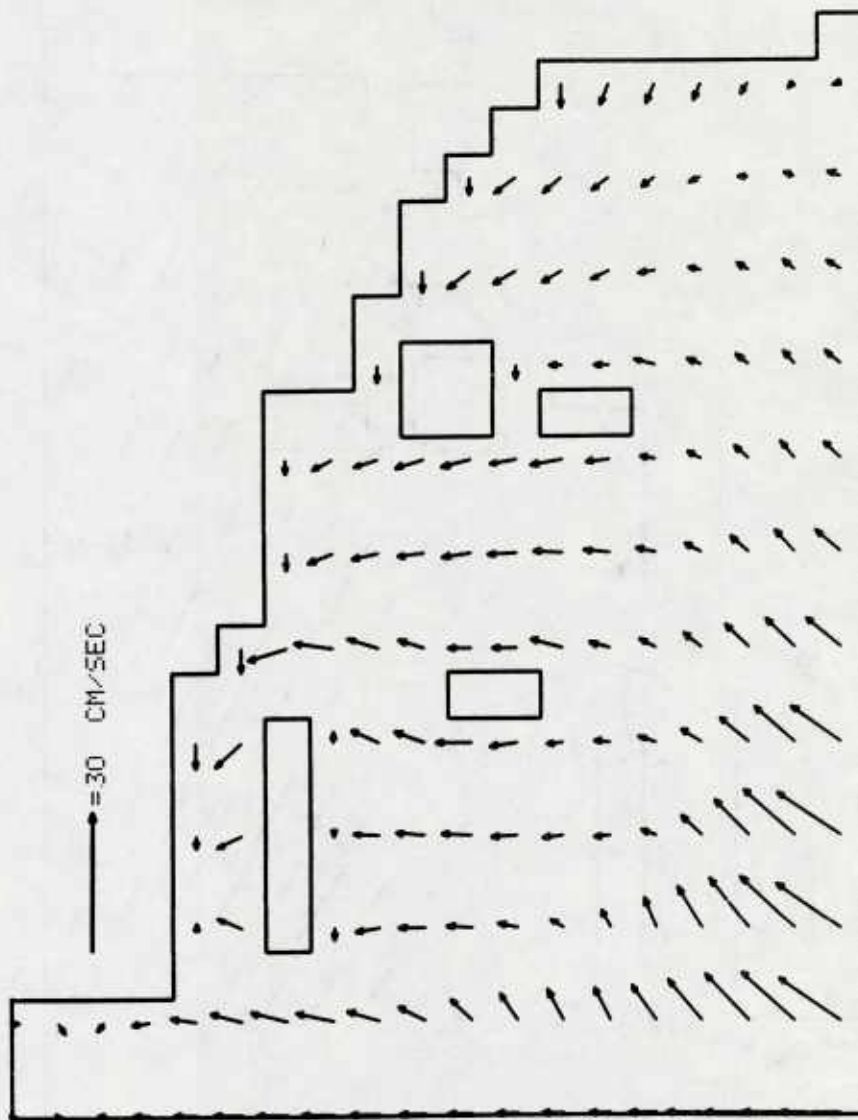
Figure 9. Currents in the surface layer during secondary high water at Long Beach.
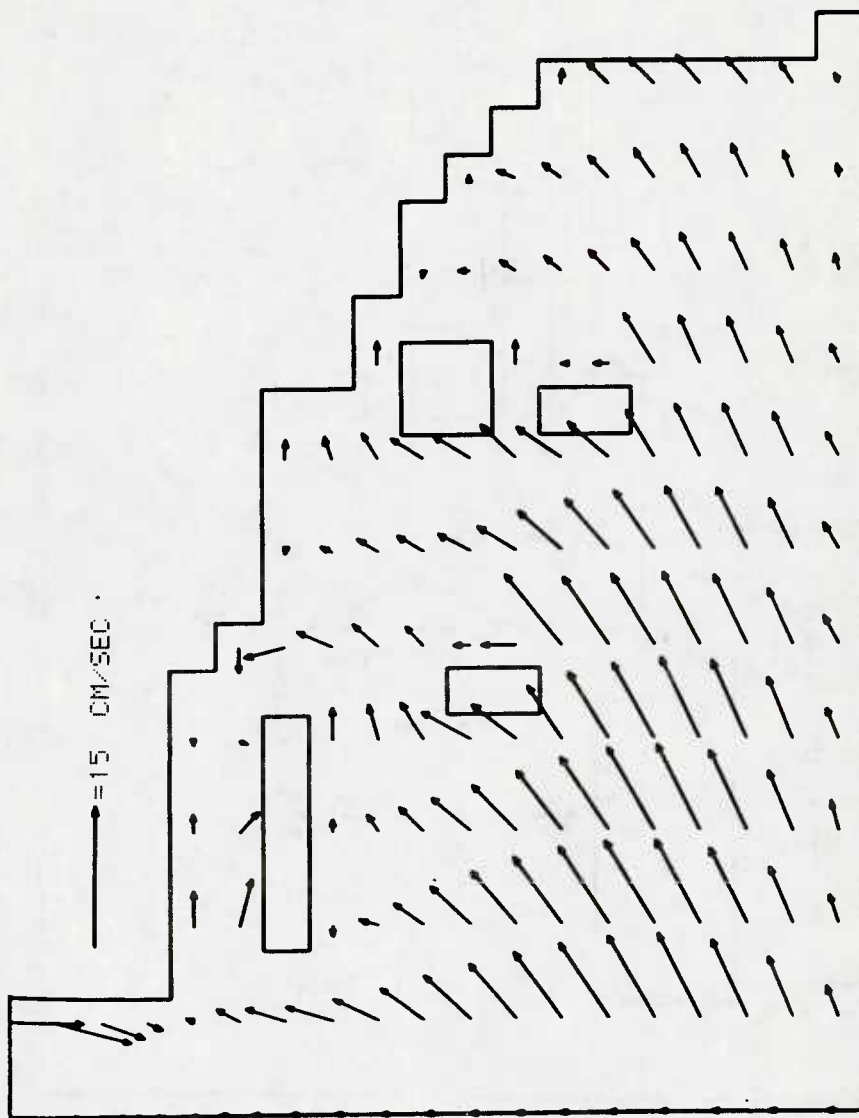
Figure 10. Currents in the intermediate layer during secondary high water at Long Beach.
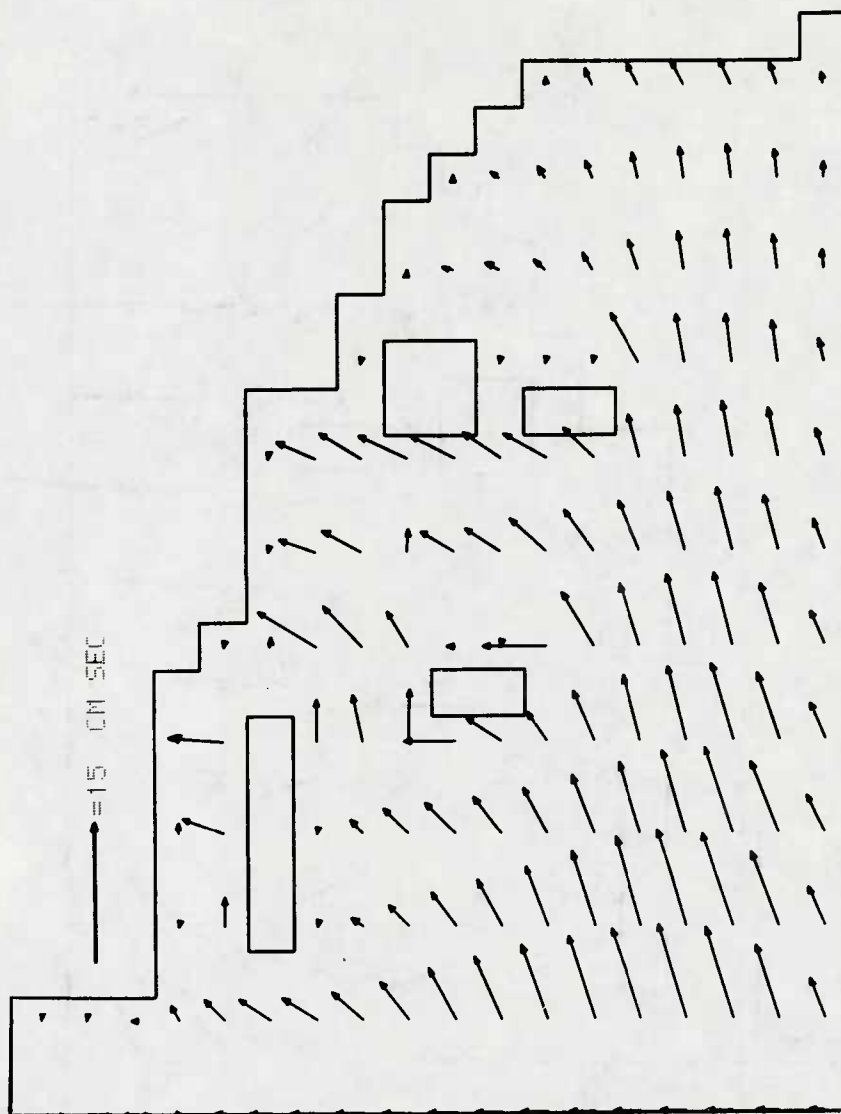
Figure 11. Currents in the bottom layer during secondary high water at Long Beach.

=15 CM/SEC
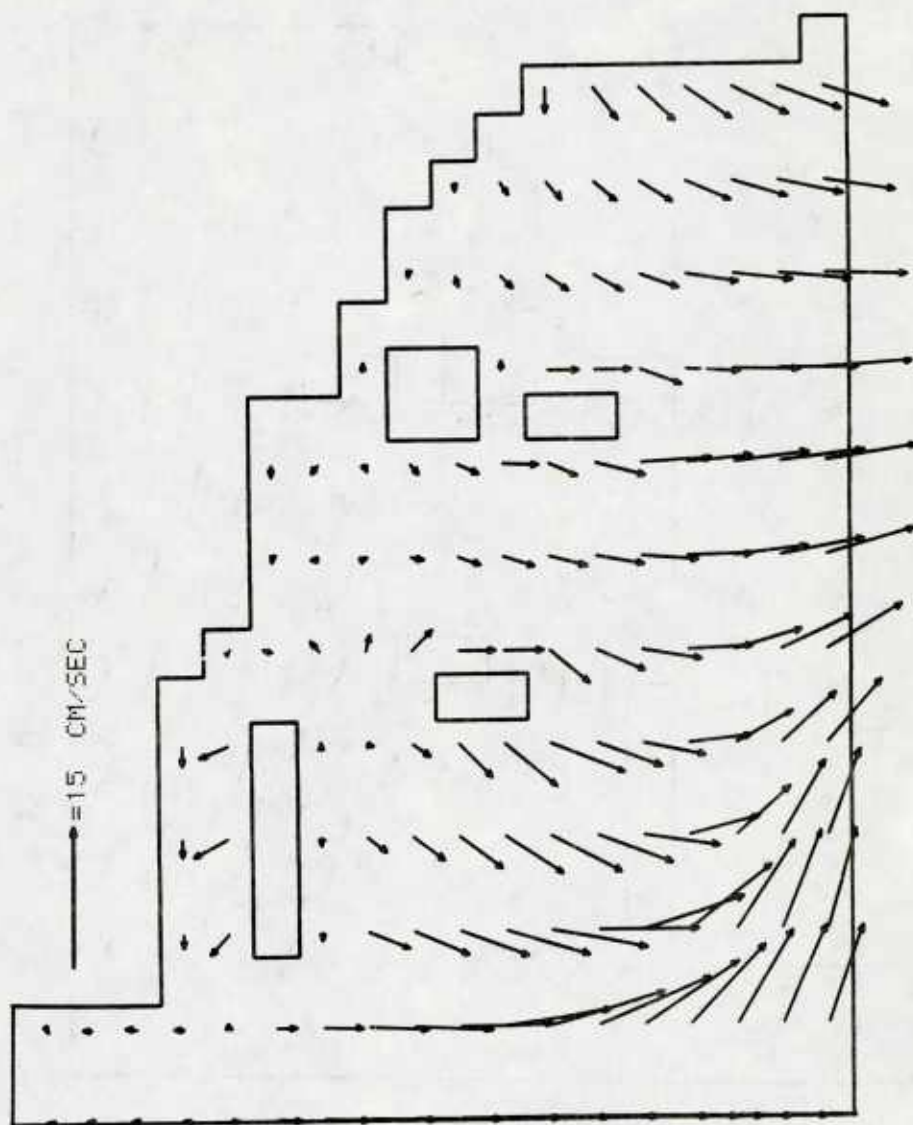
Figure 12. Currents in the surface layer 2 hours after secondary high water at Long Beach.
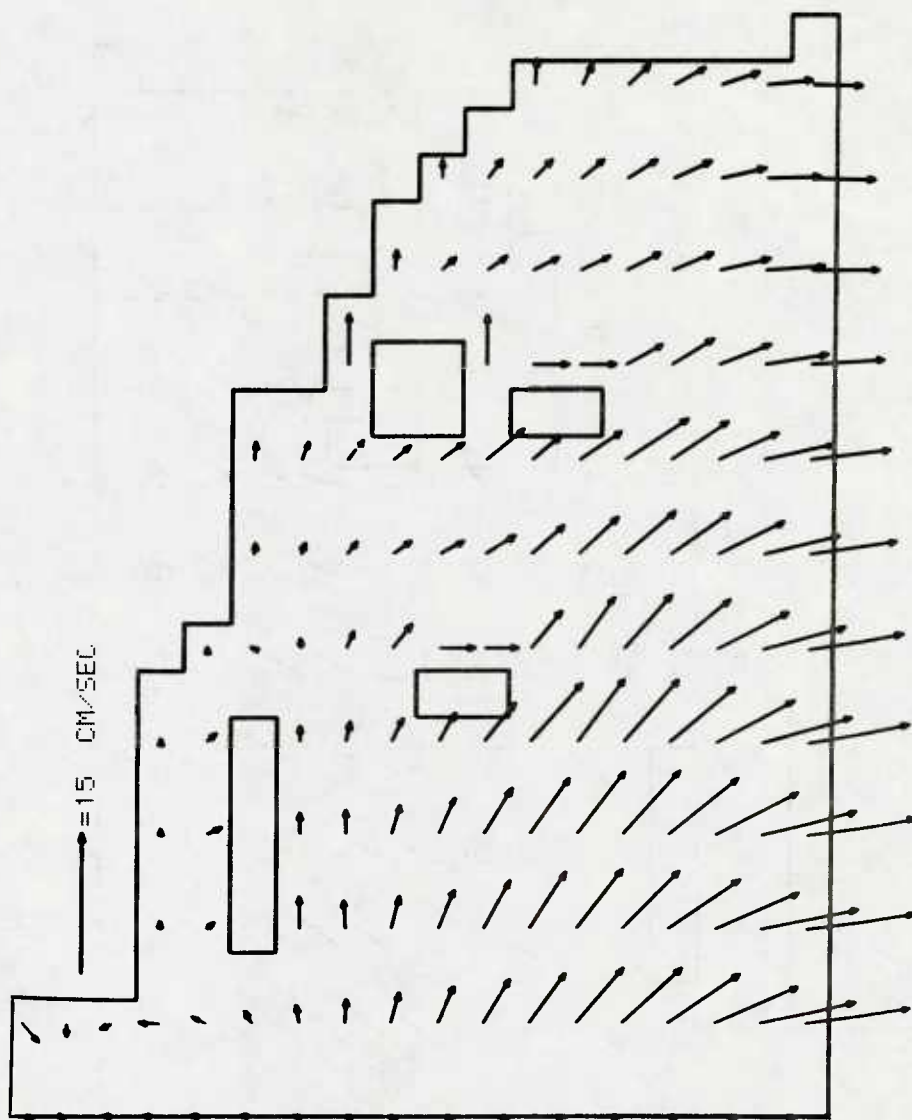
Figure 13. Currents in the intermediate layer 2 hours after secondary high water at Long Beach.

=15 CM/SEC
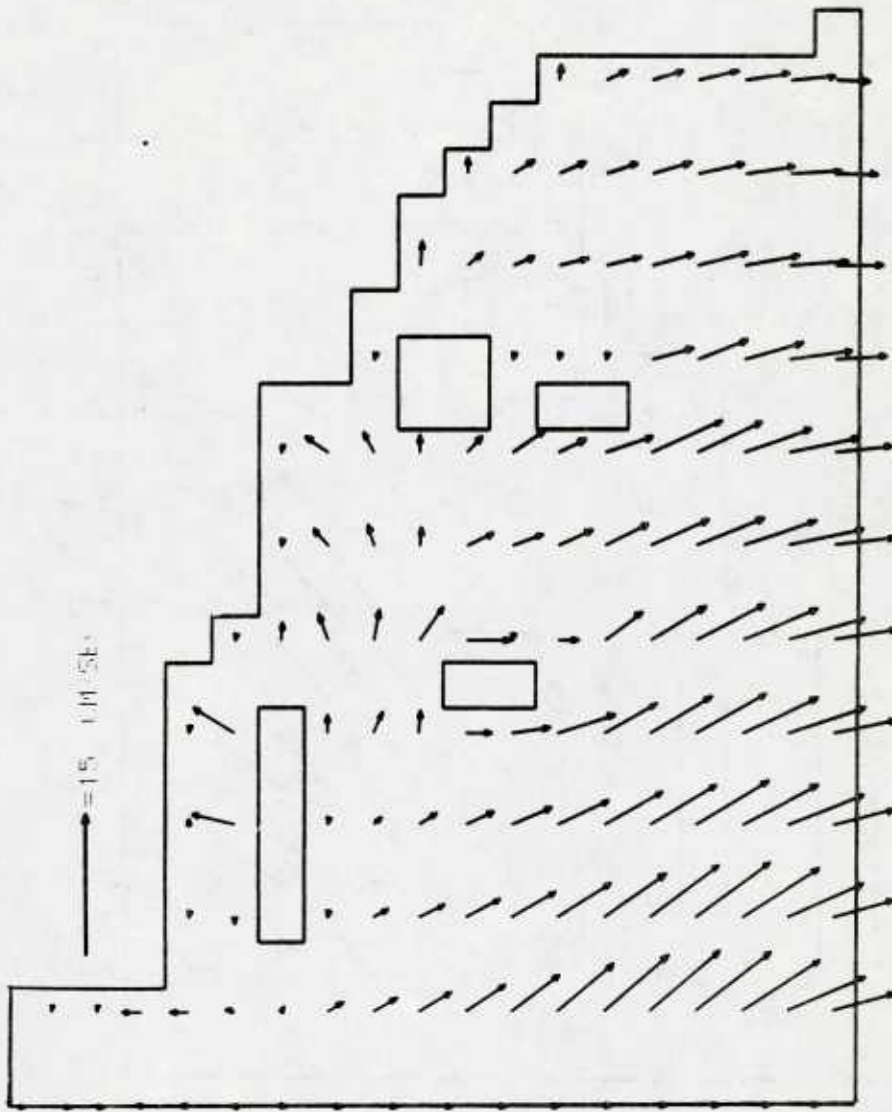
Figure 14. Currents in the bottom layer 2 hours after secondary high water at Long Beach.
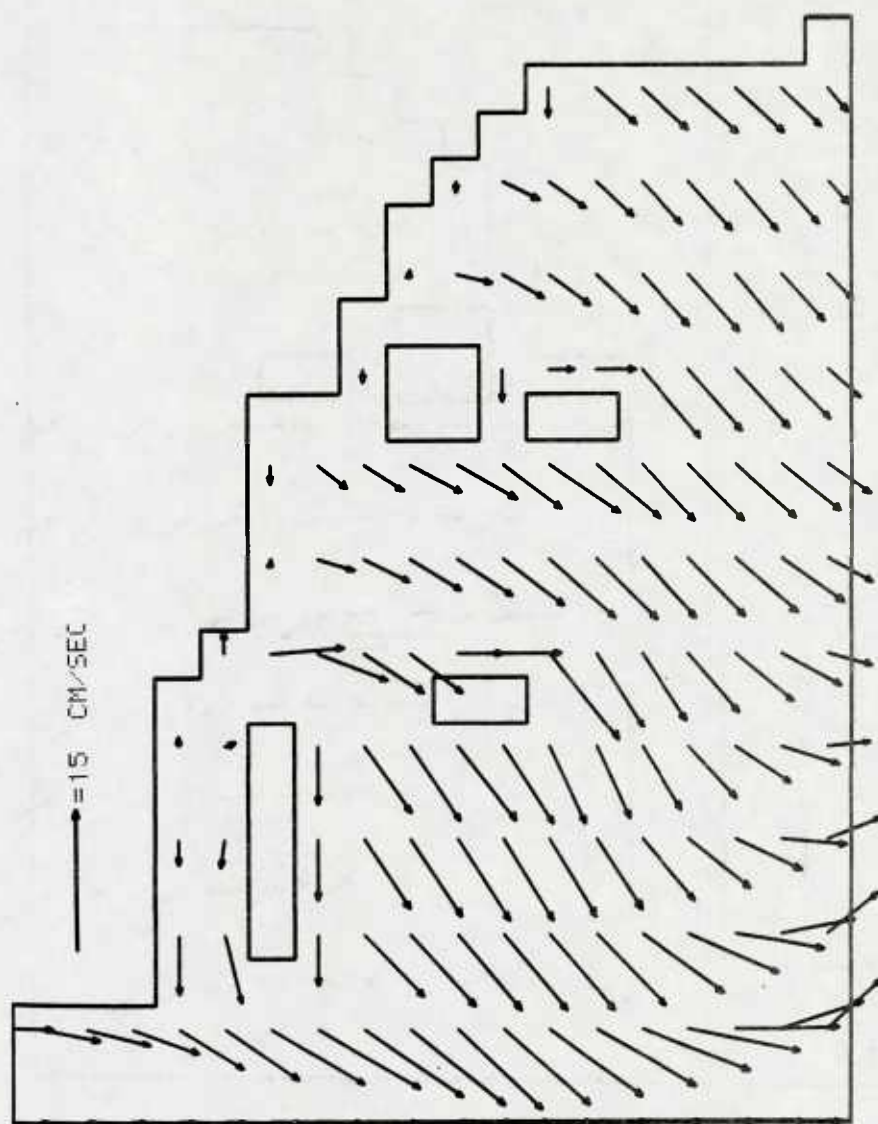
Figure 15. Currents in the surface layer during secondary low water at Long Beach.
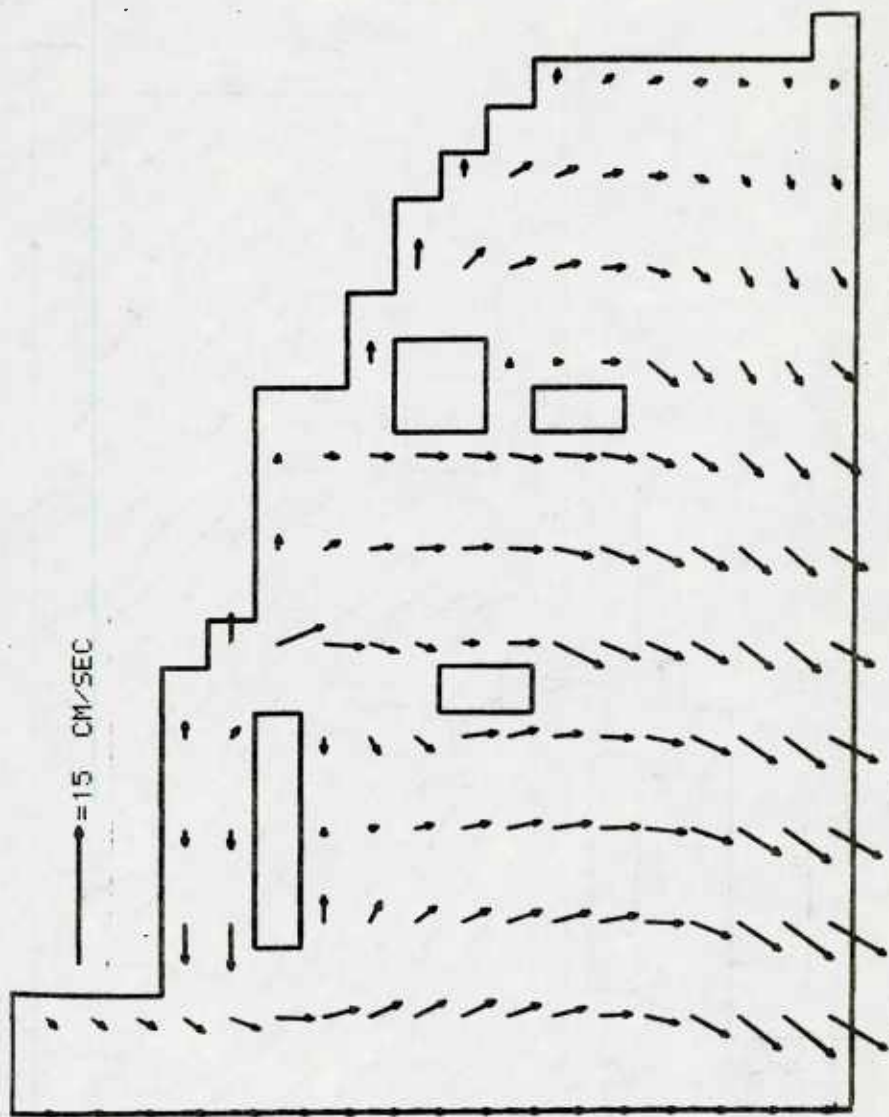
Figure 16. Currents in the intermediate layer during secondary low water at Long Beach.
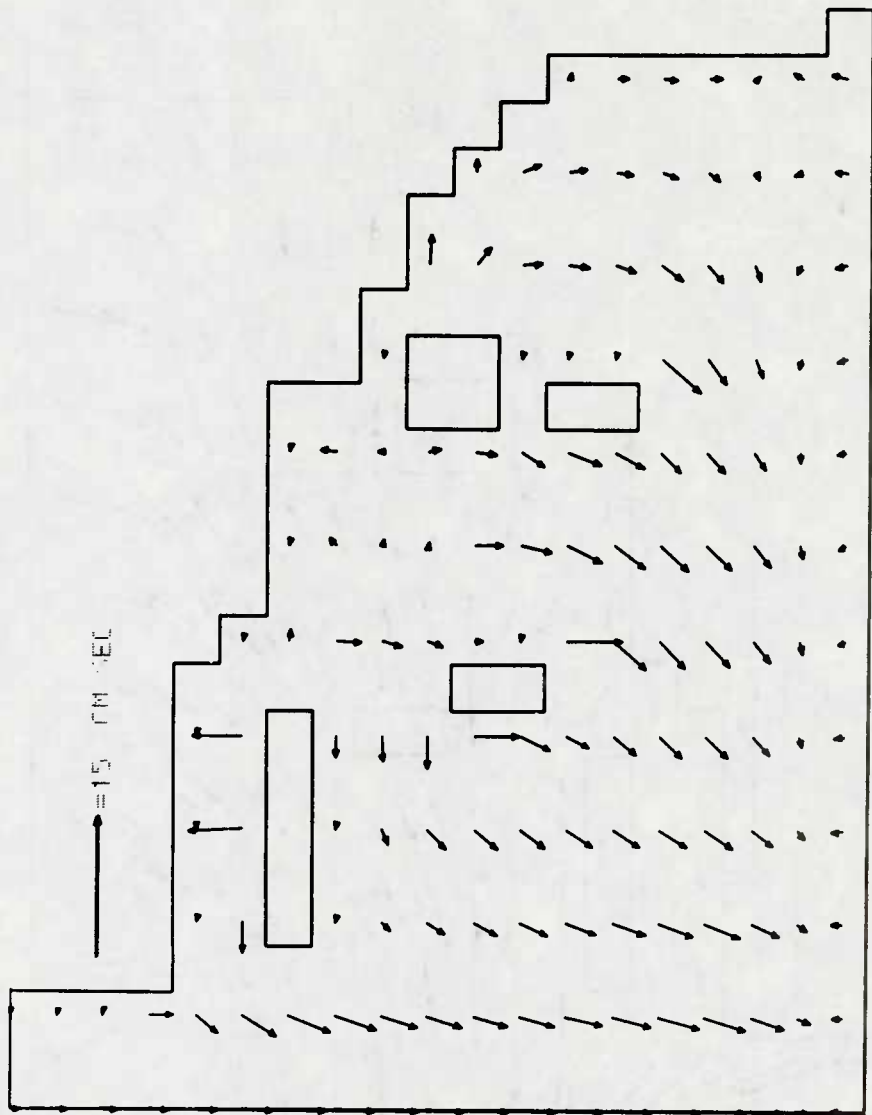
Figure 17. Currents in the bottom layer during secondary low water at Long Beach.

- 39 -
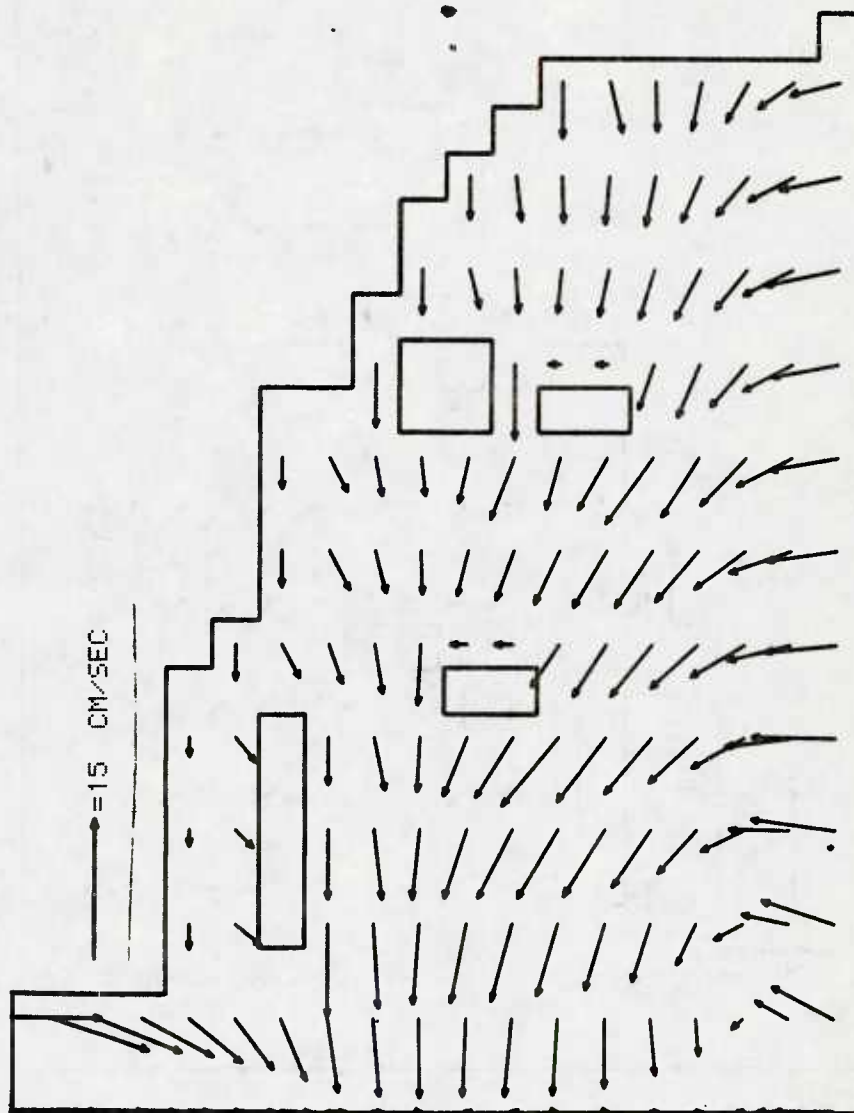
Figure 18. Currents in the surface layer 2 hours after secondary low water at Long Beach.

=15 CM/SEC
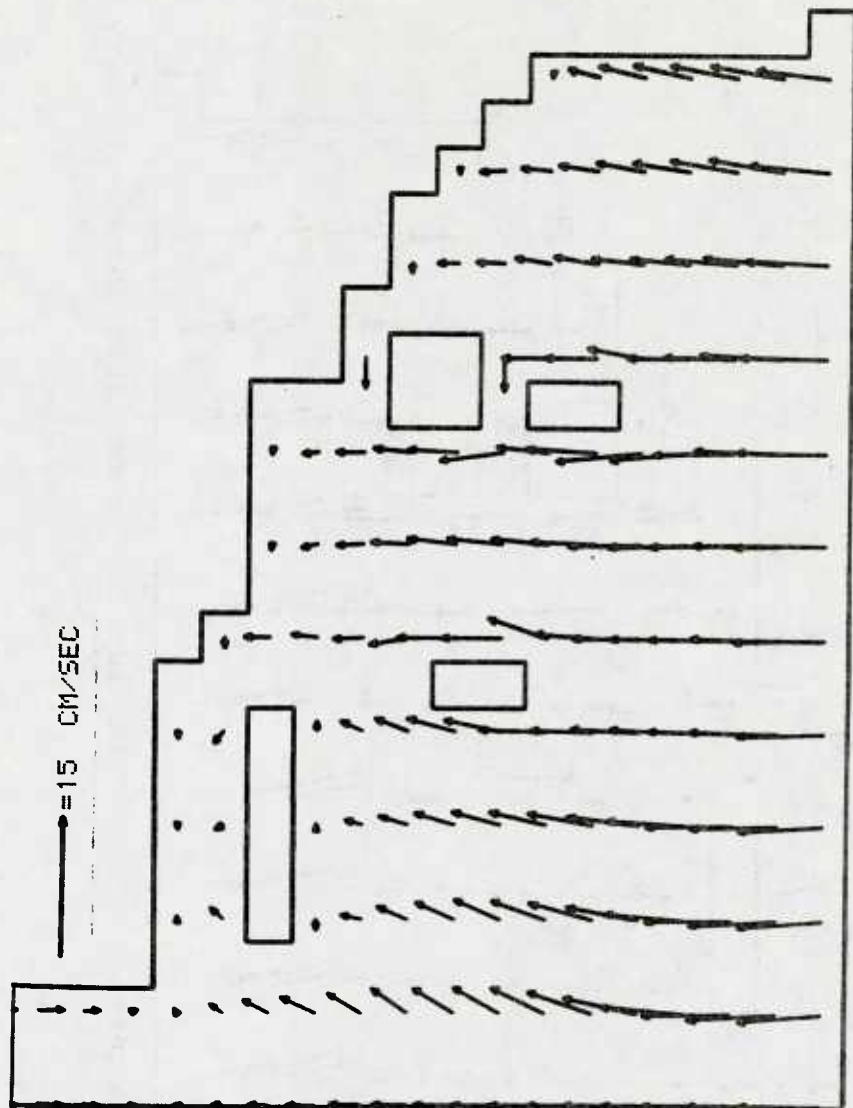
Figure 19. Currents in the intermediate layer 2 hours after secondary low water at Long Beach.

=15 CM/SEC
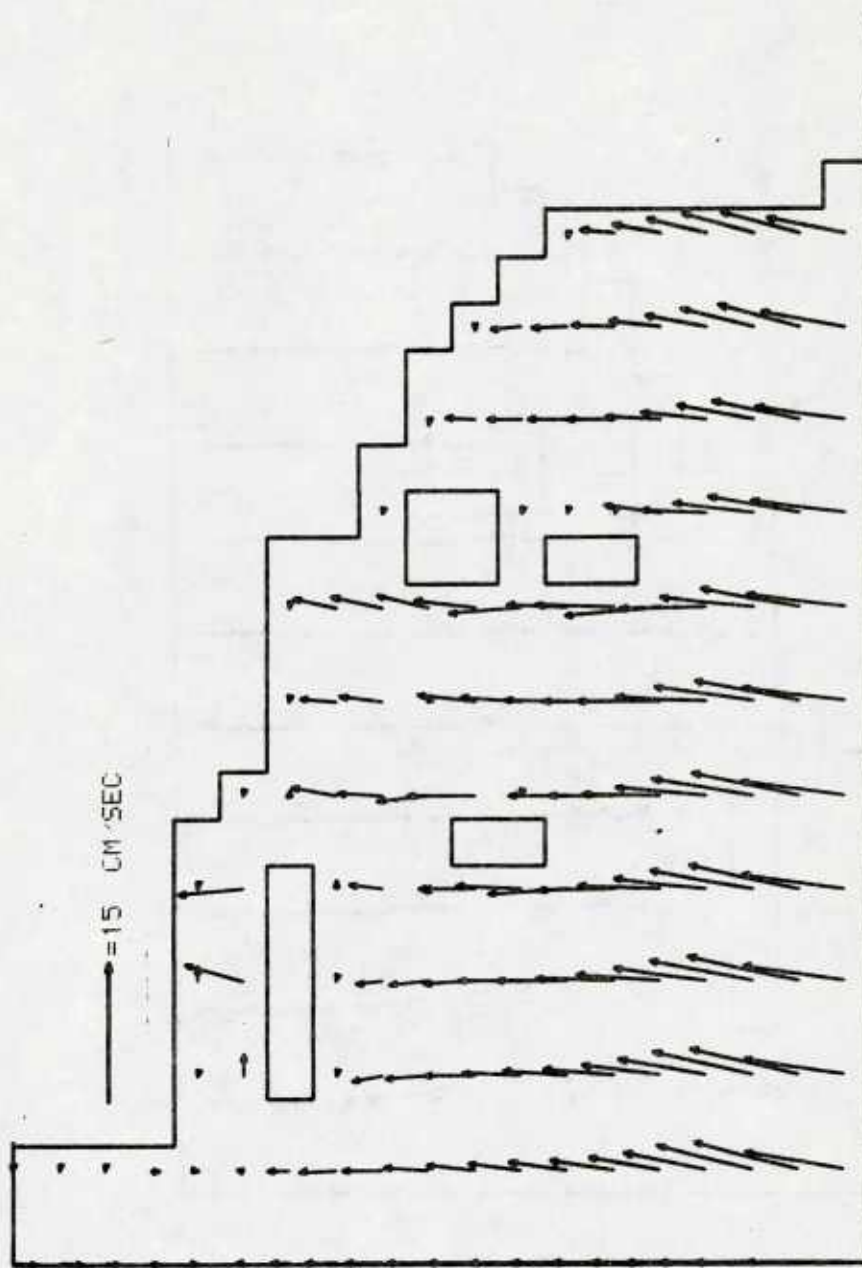
Figure 20. Currents in the bottom layer 2 hours after secondary low water at Long Beach.

=15 CM/SEC

Figure 21. Currents in the surface layer during principal high water at Long Beach.

= 30 CM/SEC
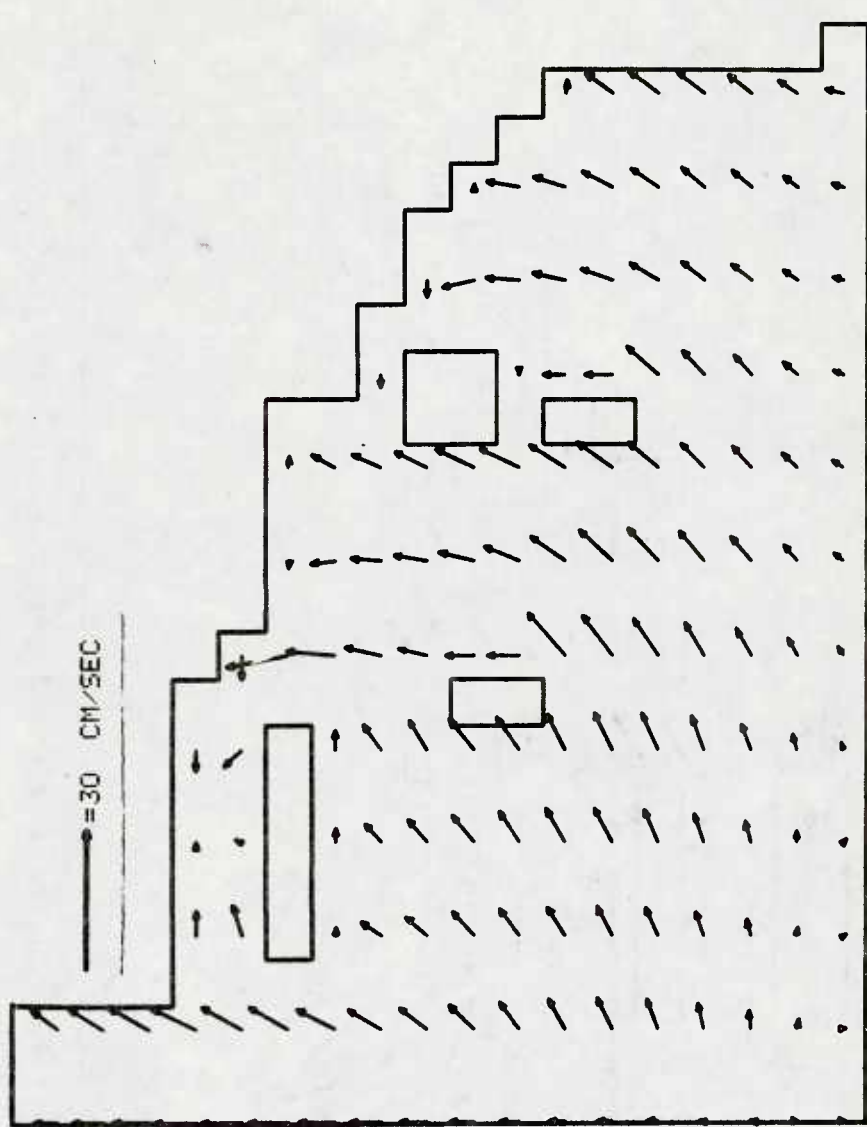
Figure 22. Currents in the intermediate layer during principal high water at Long Beach.

=30 CM/SEC

Figure 23. Currents in the bottom layer during principal high water at Long Beach.
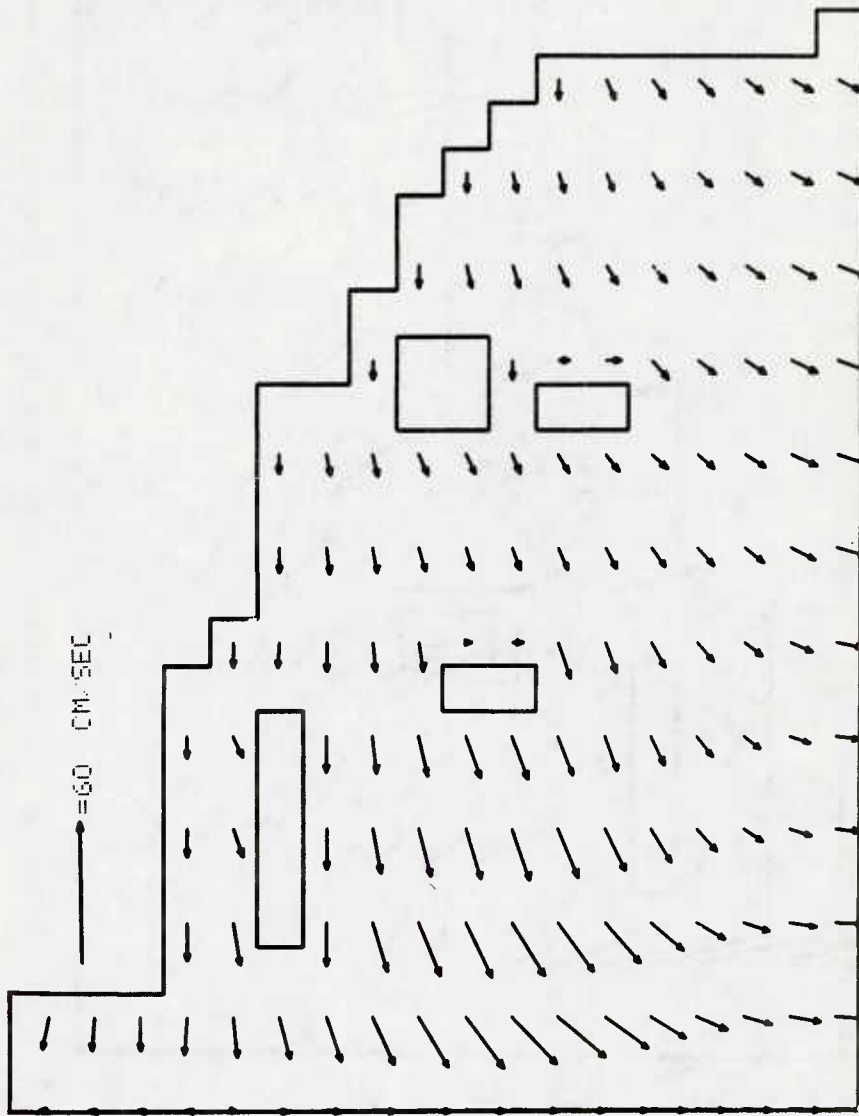
Figure 24. Currents in the surface layer 2 hours after principal high water at Long Beach.
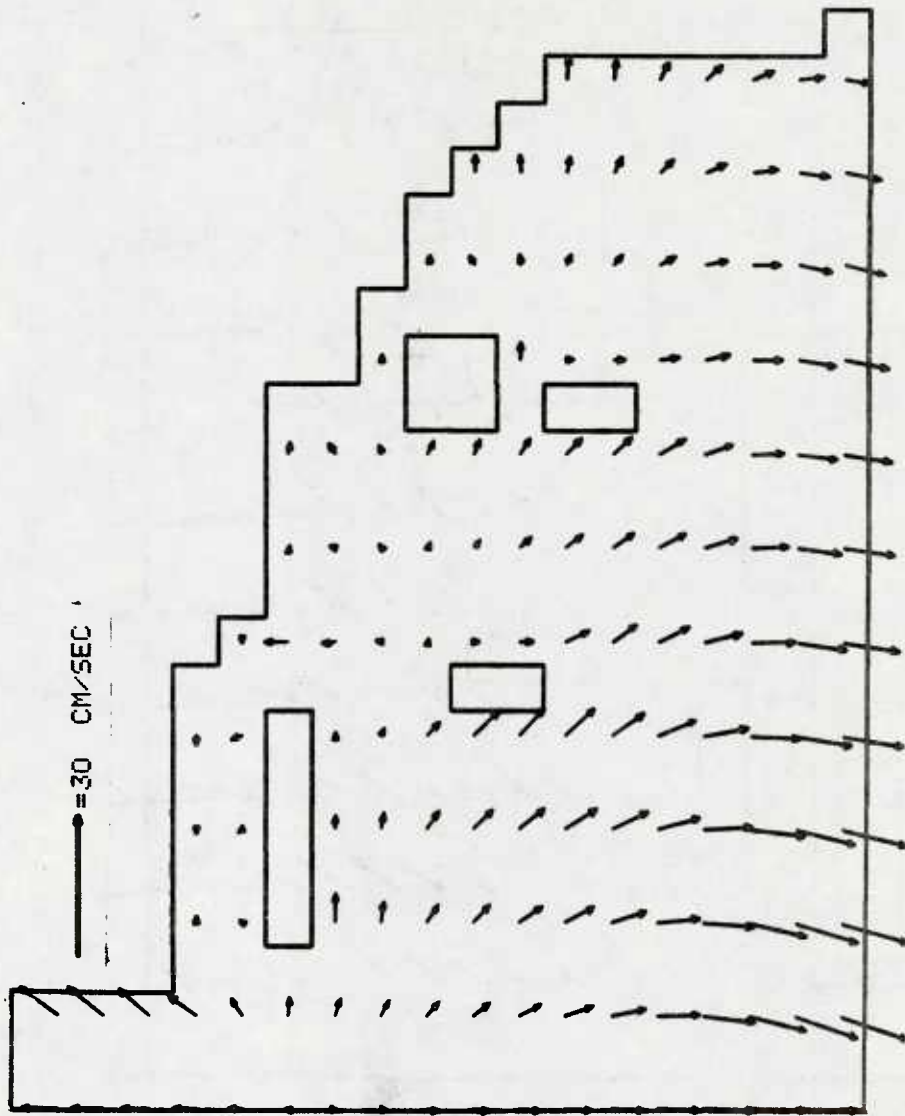
Figure 25. Currents in the intermediate layer 2 hours after principal high water at Long Beach.

- 47 -
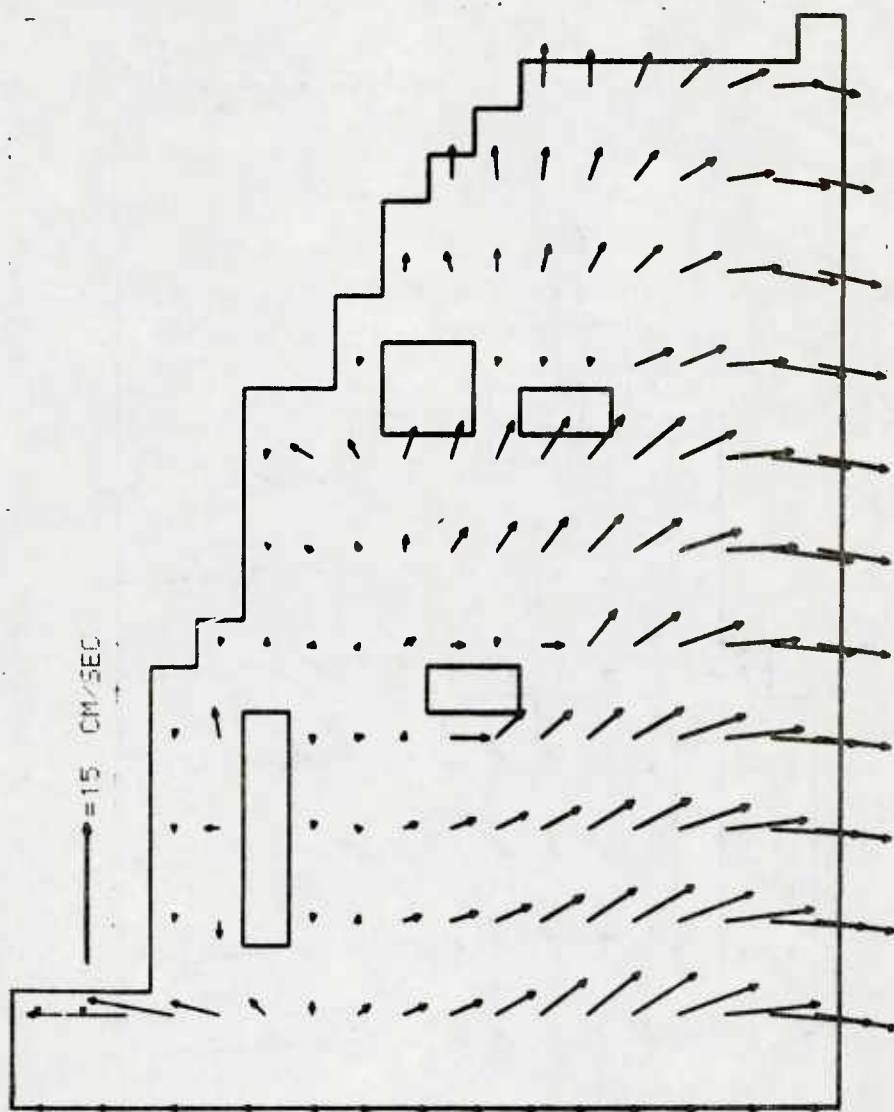
Figure 26. Currents in the bottom layer 2 hours after principal high water at Long Beach.

=15 CM/SEC
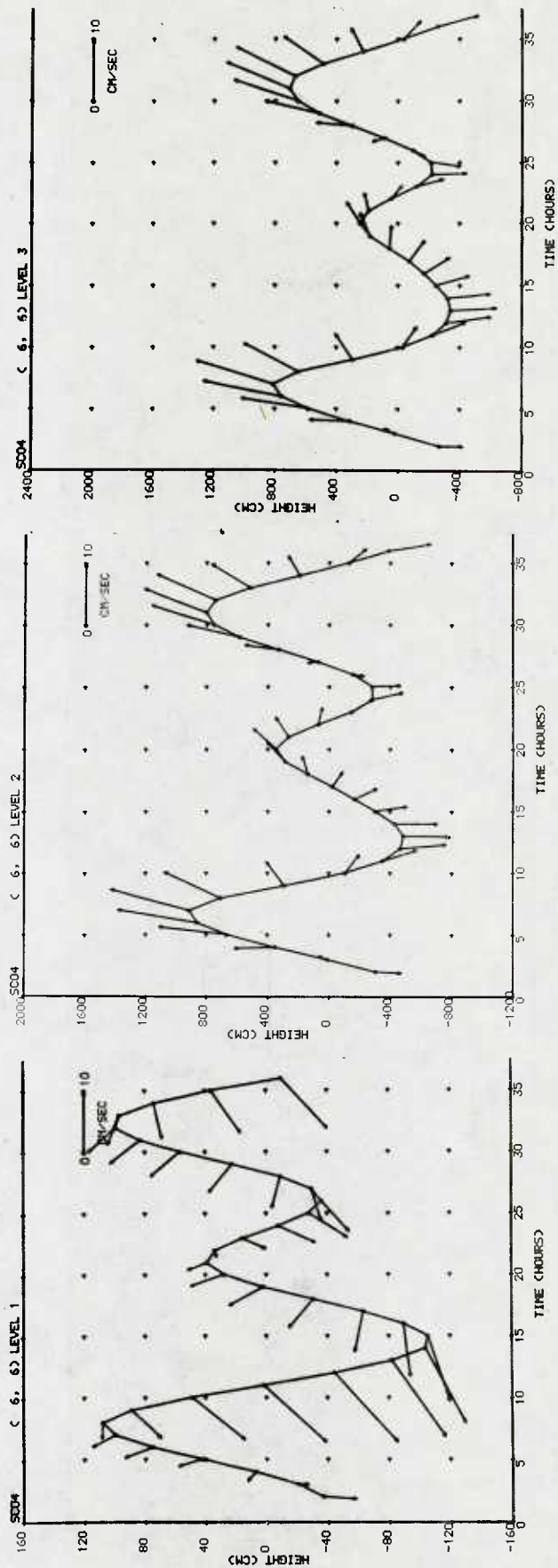
Figure 27. Currents and sea level and interface depth changes at special output point 1 (see Figure 1 for location).
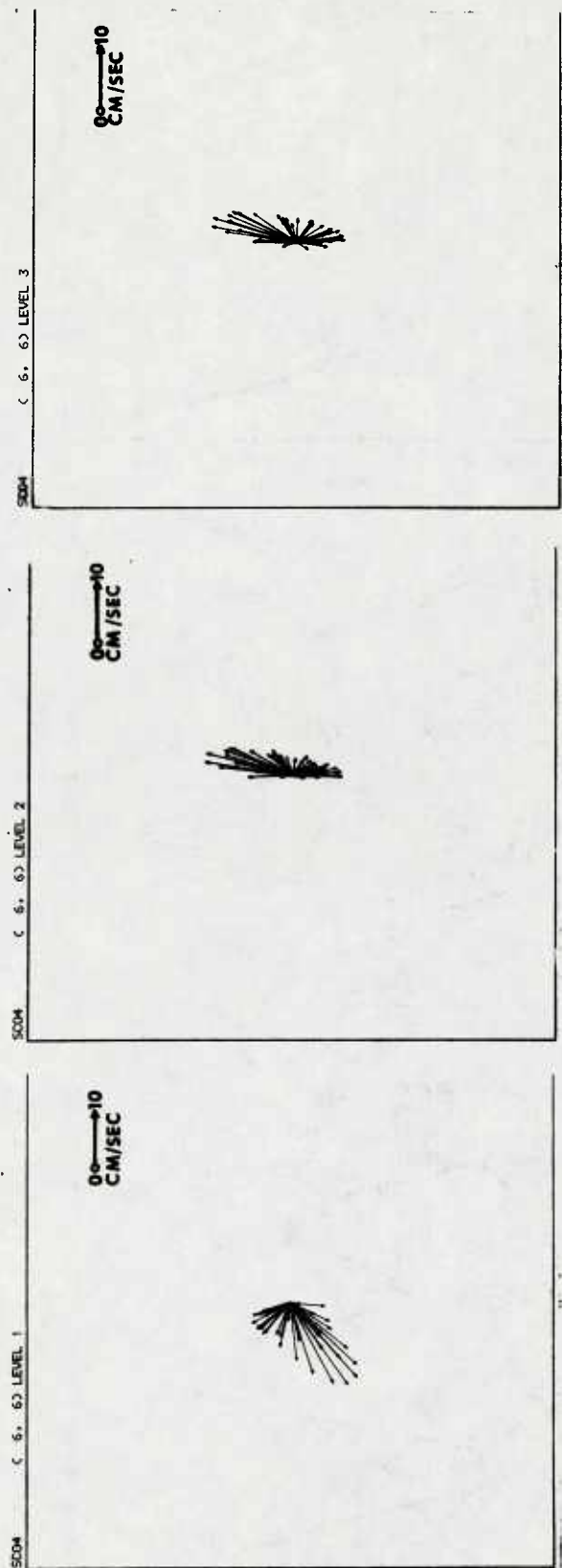
Figure 28. Current roses for three different layers at special output point 1 (see Figure 1 for location).
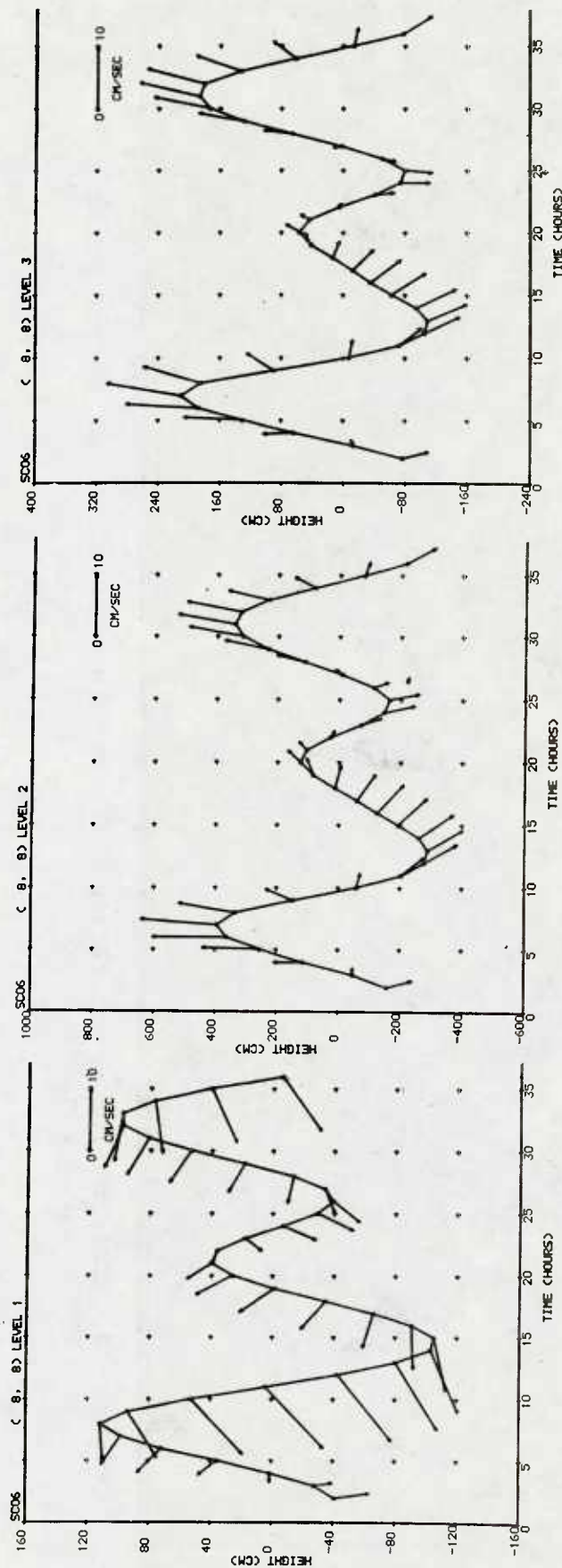
Figure 29. Currents and sea level and interface depth changes at special output point 2 (see Figure 1 for location).
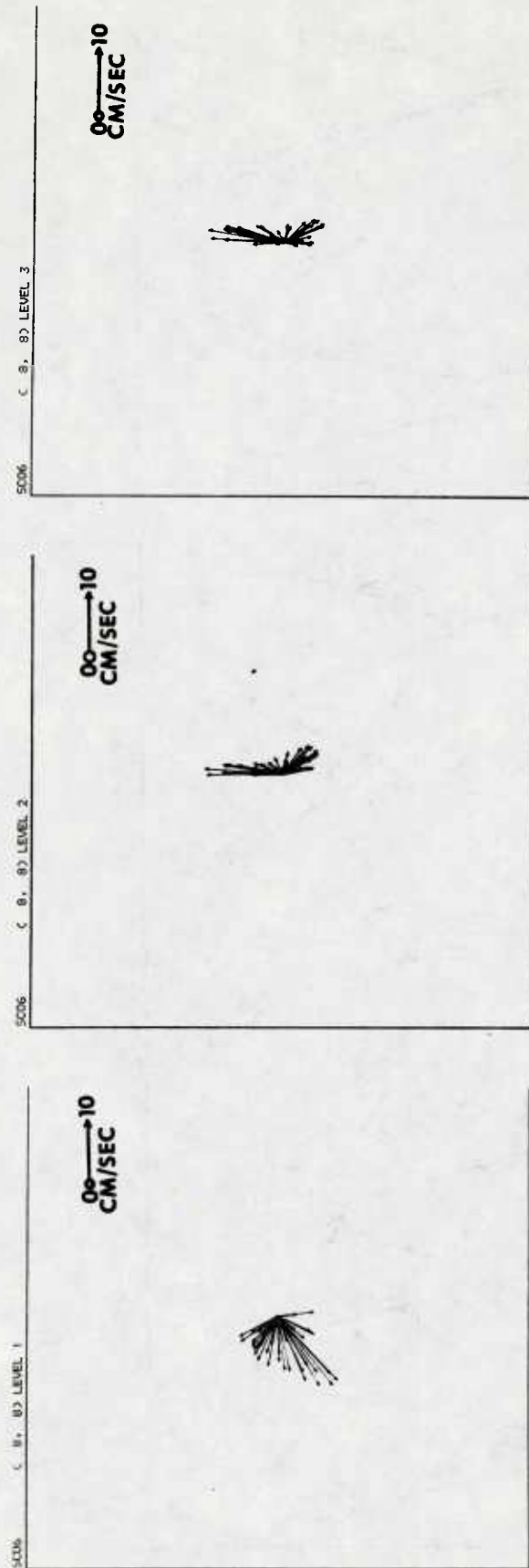
Figure 30. Current roses for three different layers at special output point 2 (see Figure 1 for location).
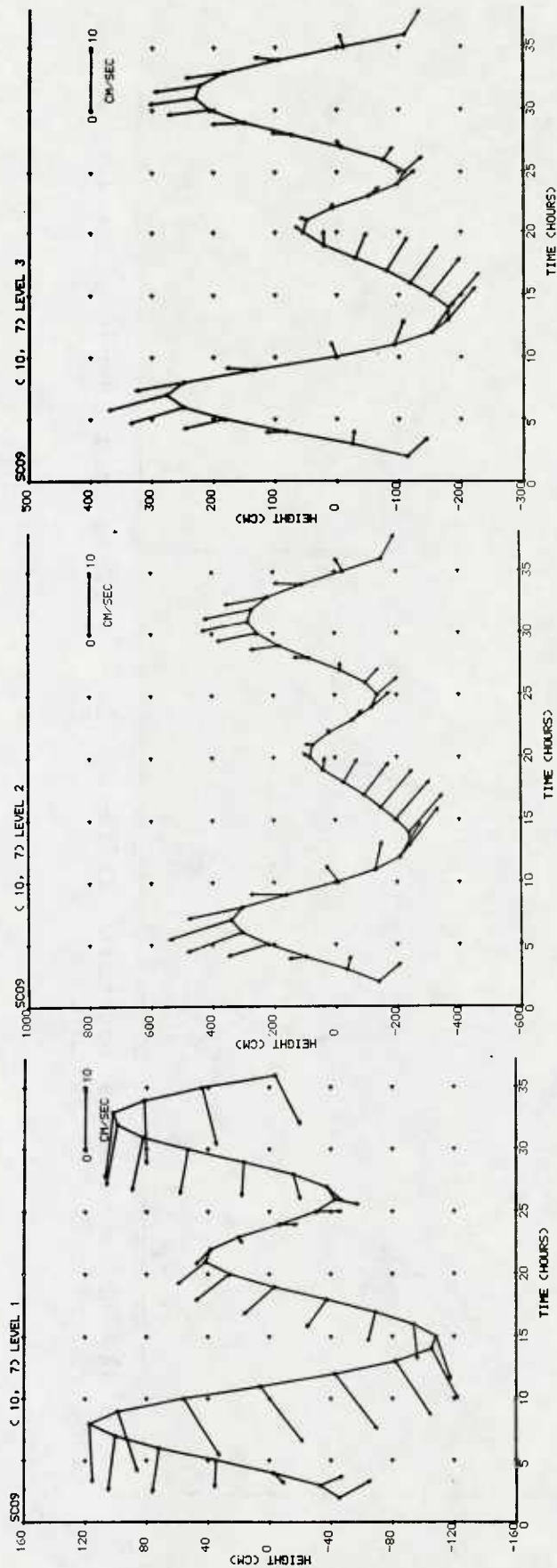
Figure 31. Currents and sea level and interface depth changes at special output point 4 (see Figure 1 for location).
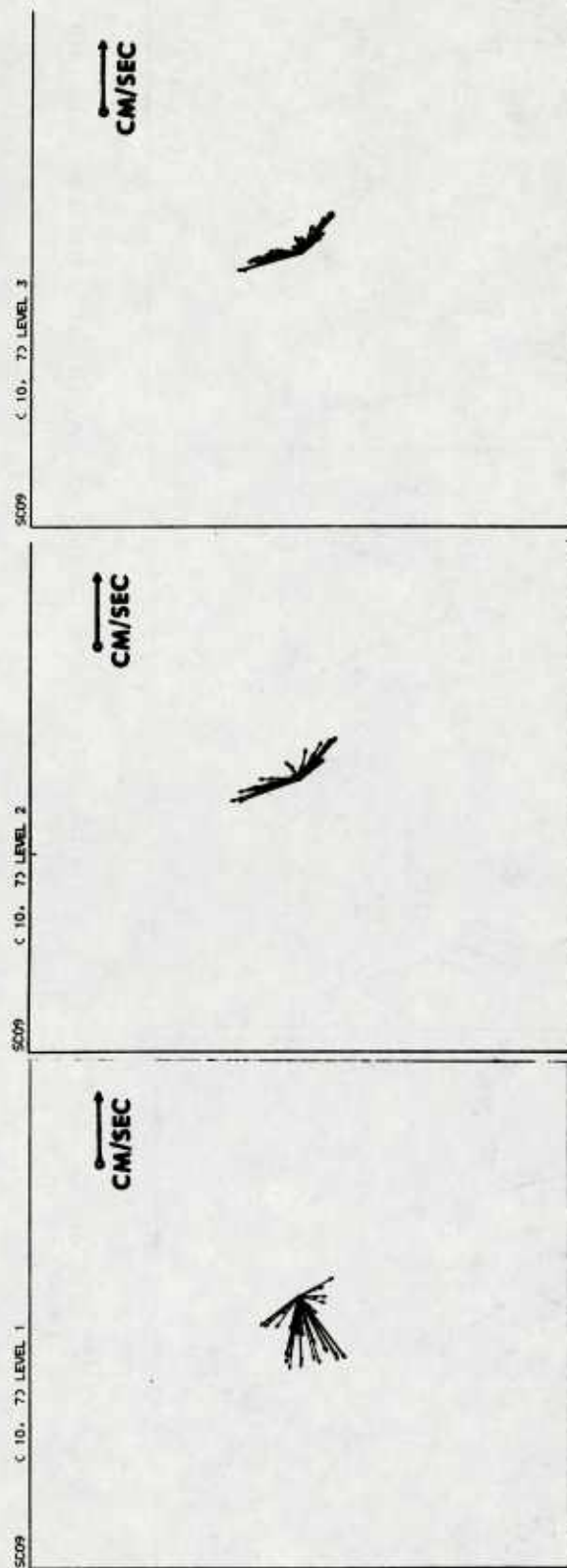
Figure 32. Current roses for three different layers at special output point 4 (see Figure 1 for location).

- 54 -
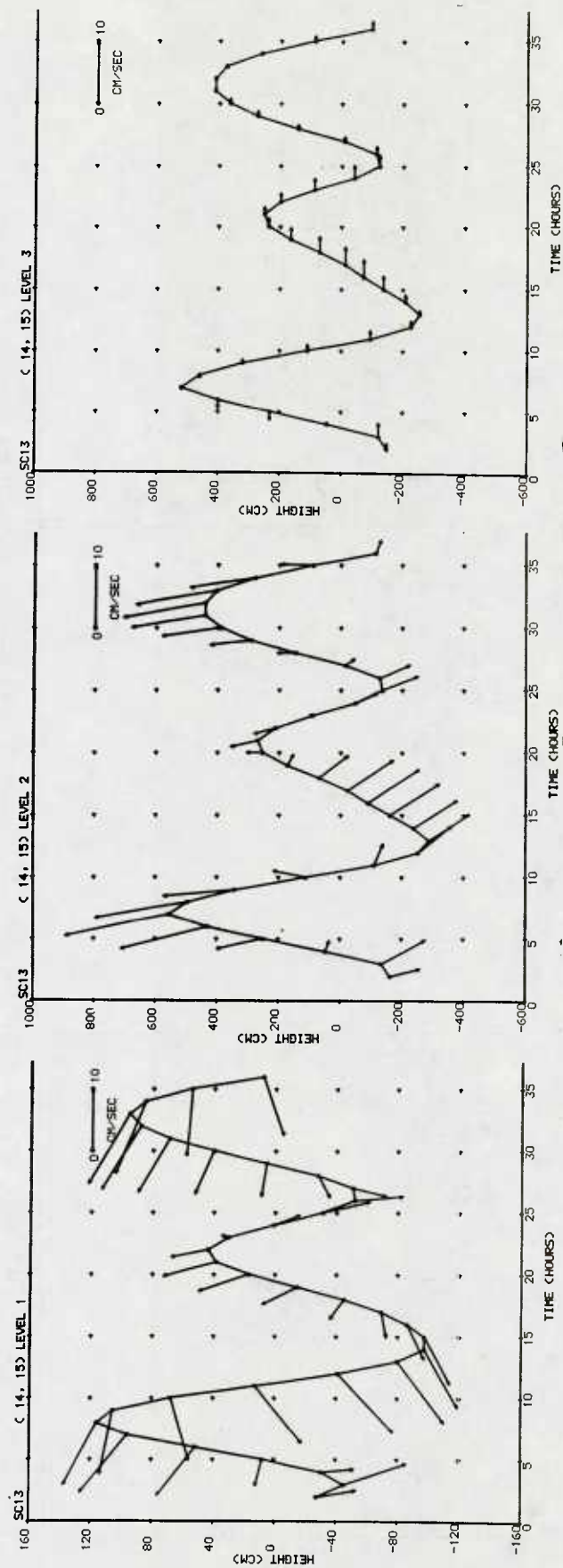
Figure 33. Currents and sea level and interface depth changes at special output point 5 (see Figure 1 for location).

- 55 -
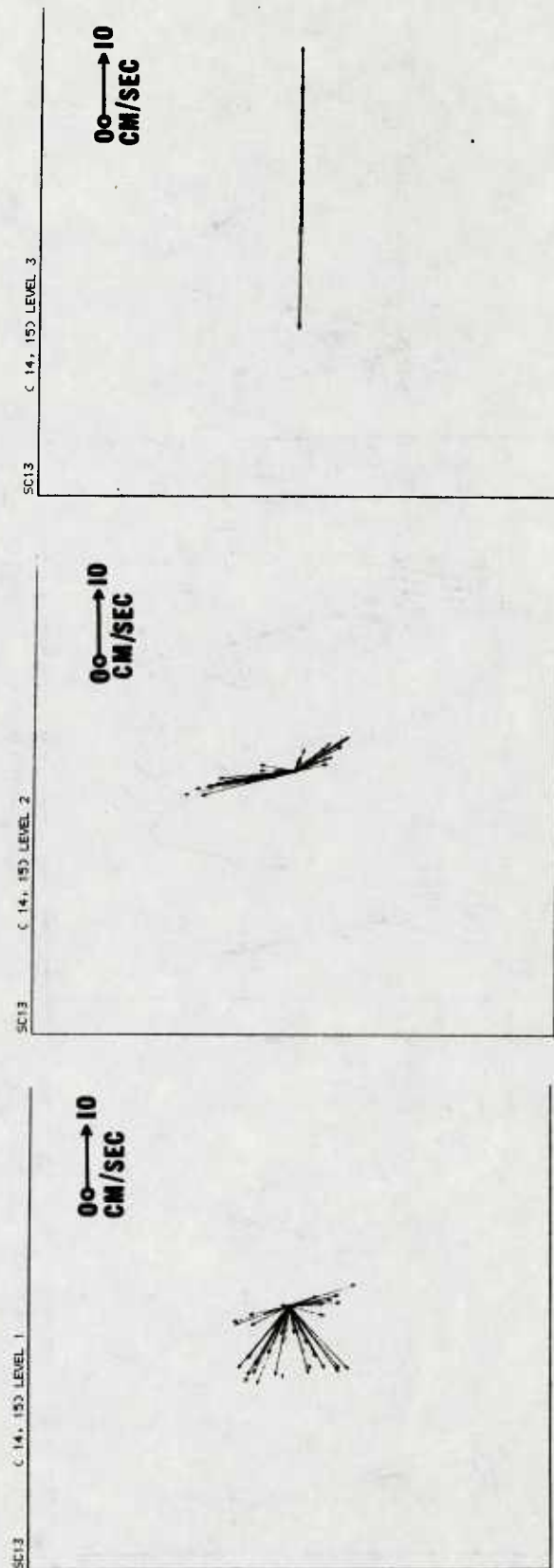
Figure 34. Current roses for three different layers at special output point 5 (see Figure 1 for location).
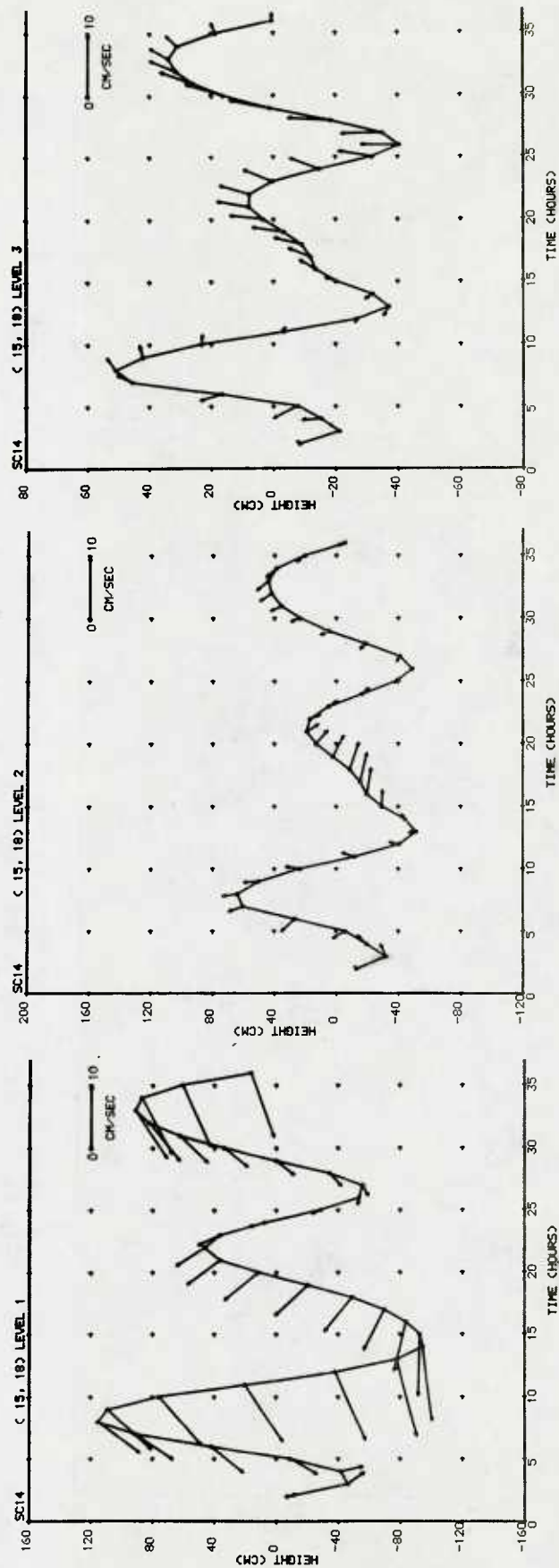
Figure 35. Currents and sea level and interface depth changes at special output point 6 (see Figure 1 for location).
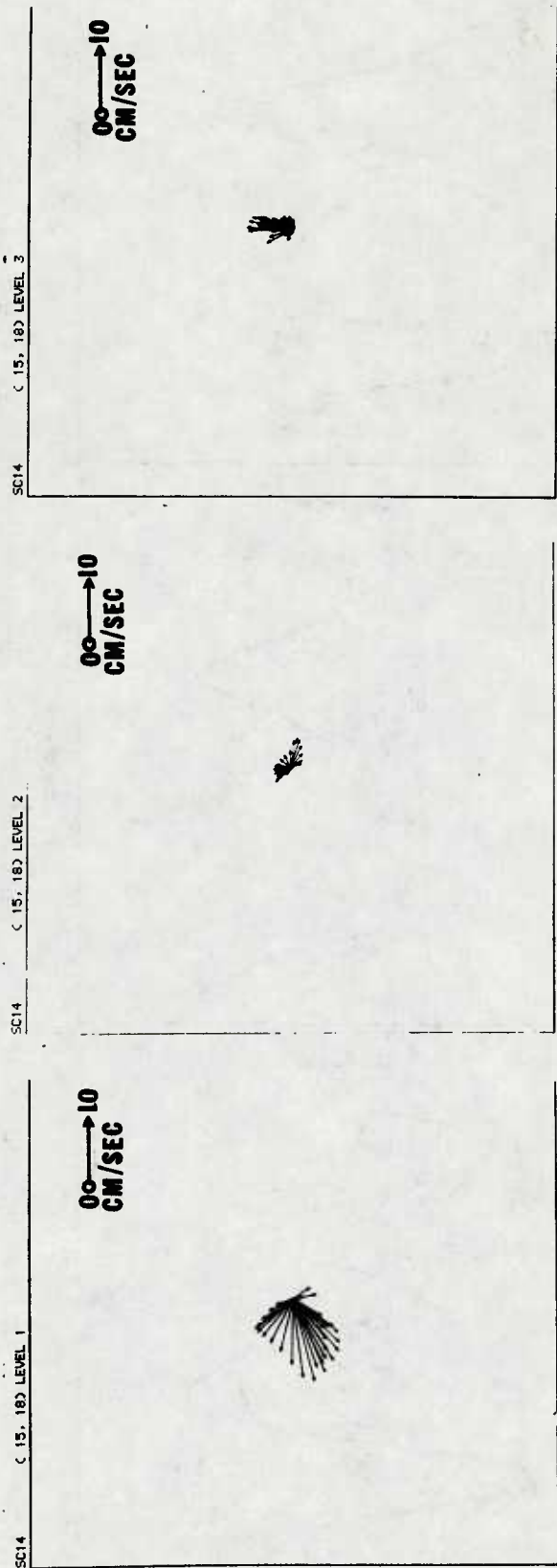
Figure 36. Current roses for three different layers at special output point 6 (see Figure 1 for location).
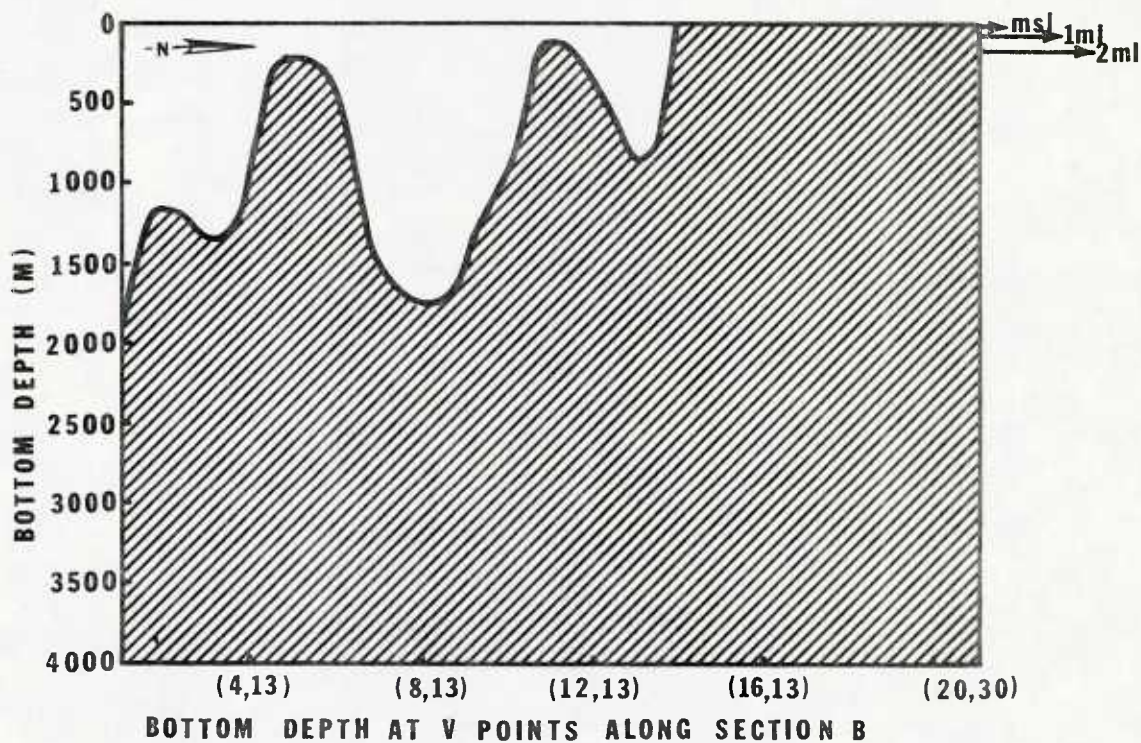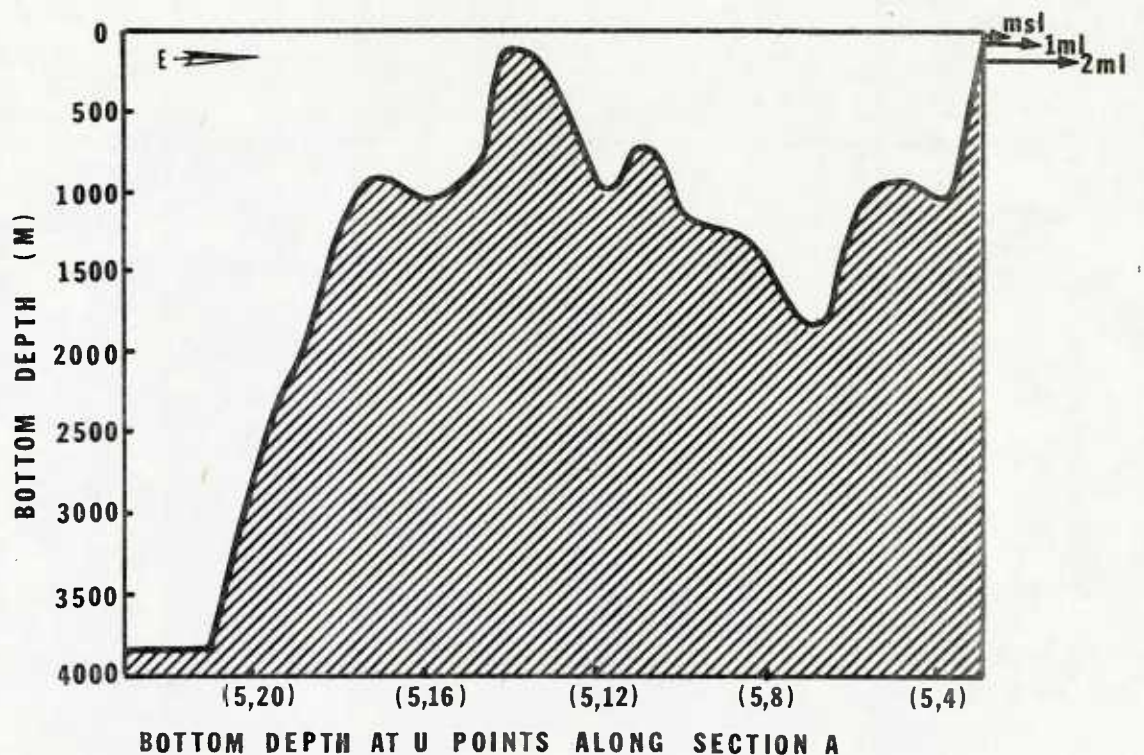
Figure 37. Water depths along sections A and B (for locations of the sections, see Figure 1).
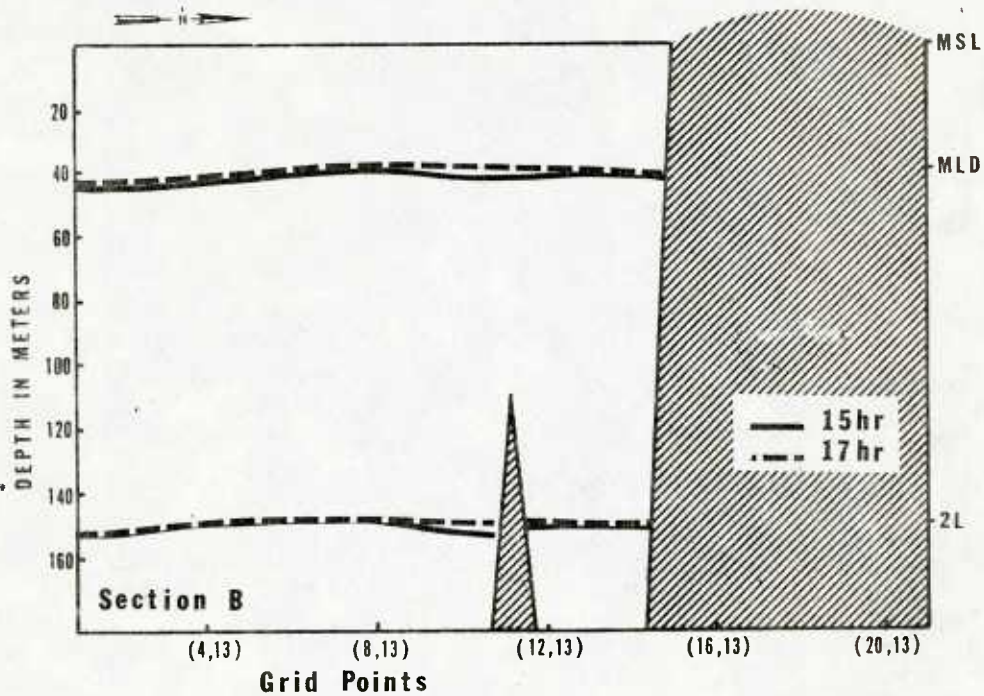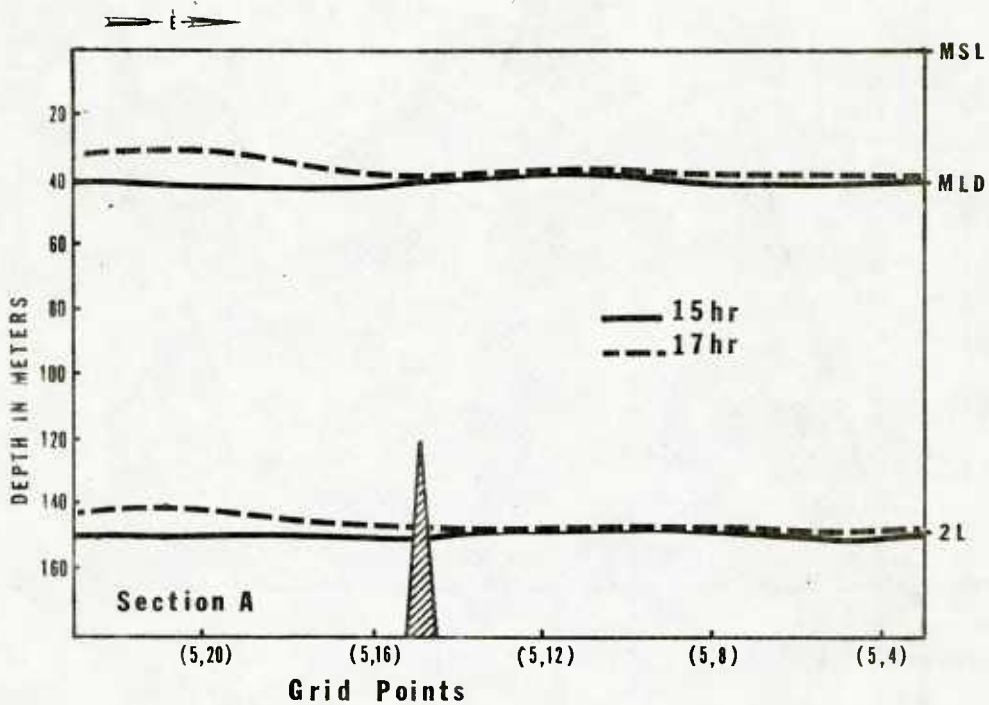
Figure 38. Depth of layer interfaces along sections A and B during and 2 hours after principal low water at Long Beach.
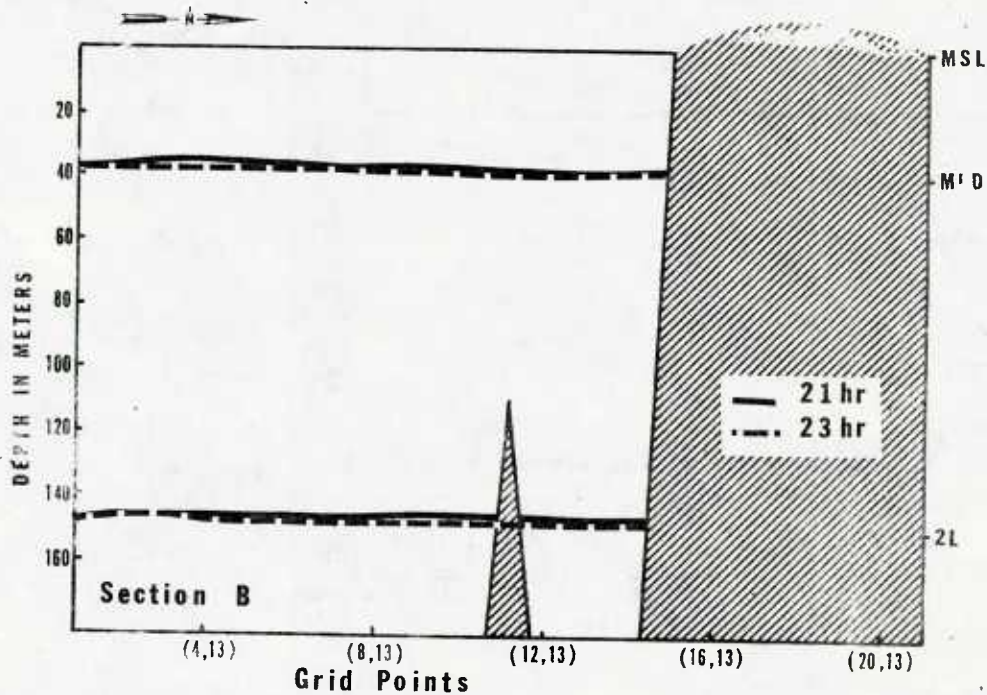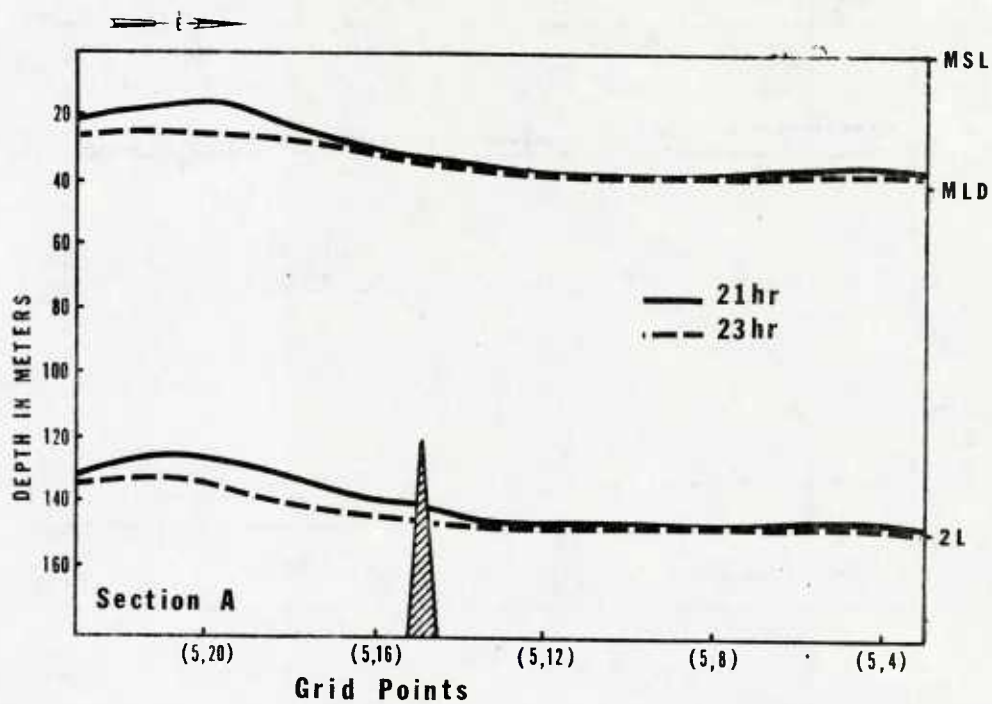
Figure 39. Depth of layer interfaces along sections A and B during and 2 hours after secondary high water at Long Beach.
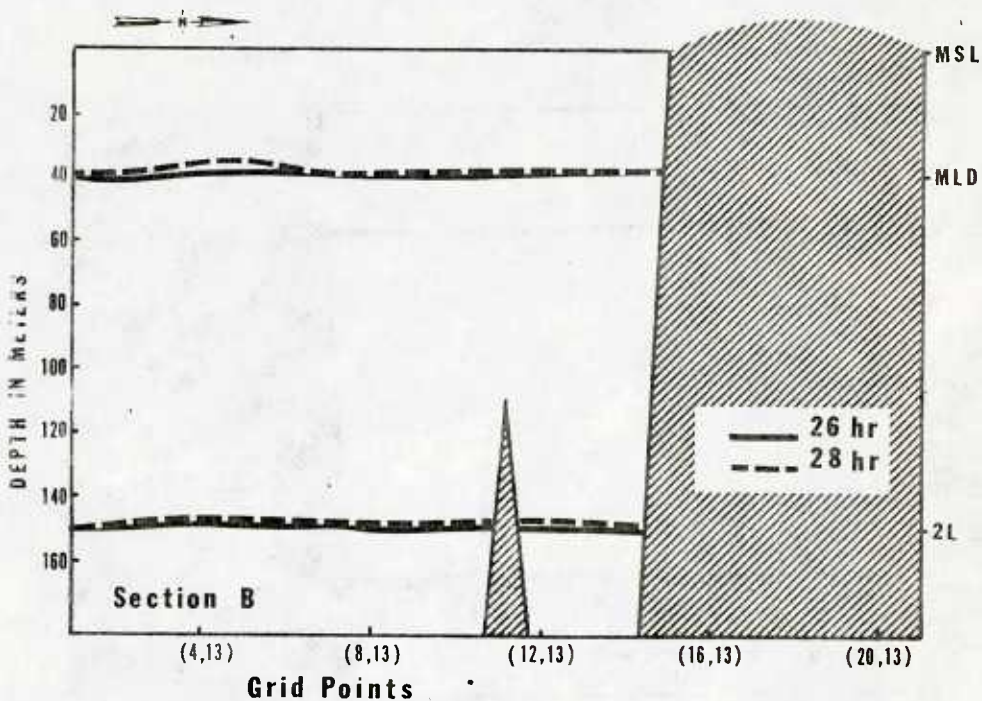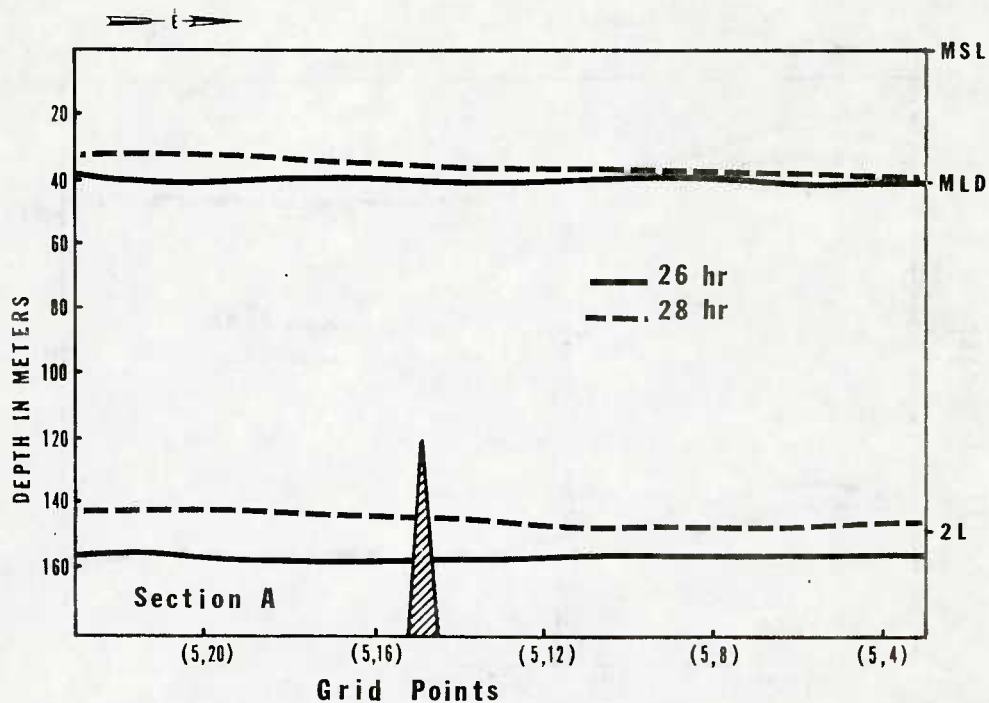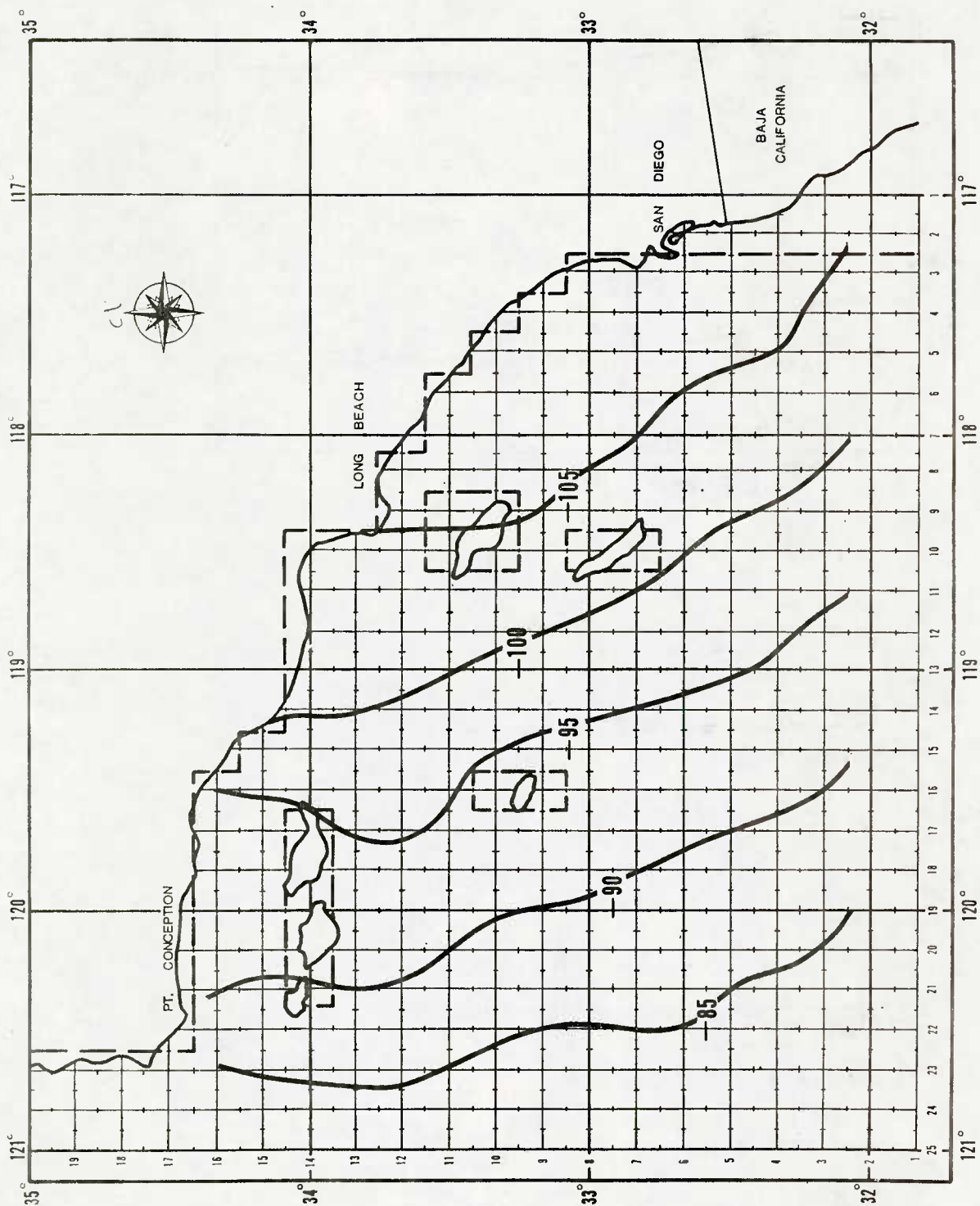
Figure 40. Depth of layer interfaces along sections A and B
during and 2 hours after secondary low water at Long Beach.
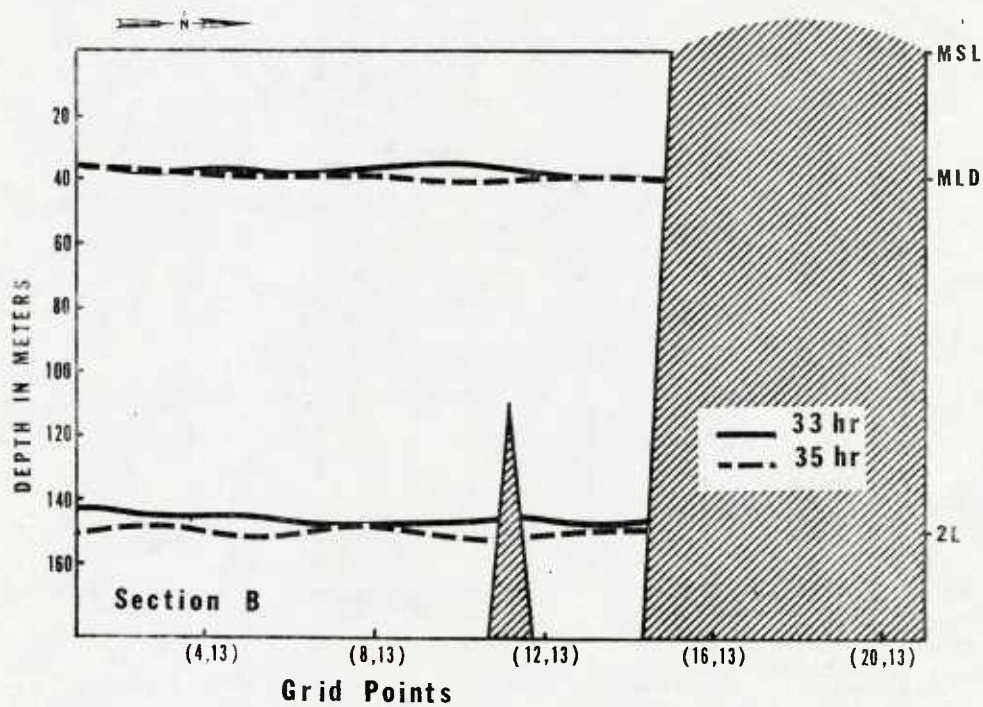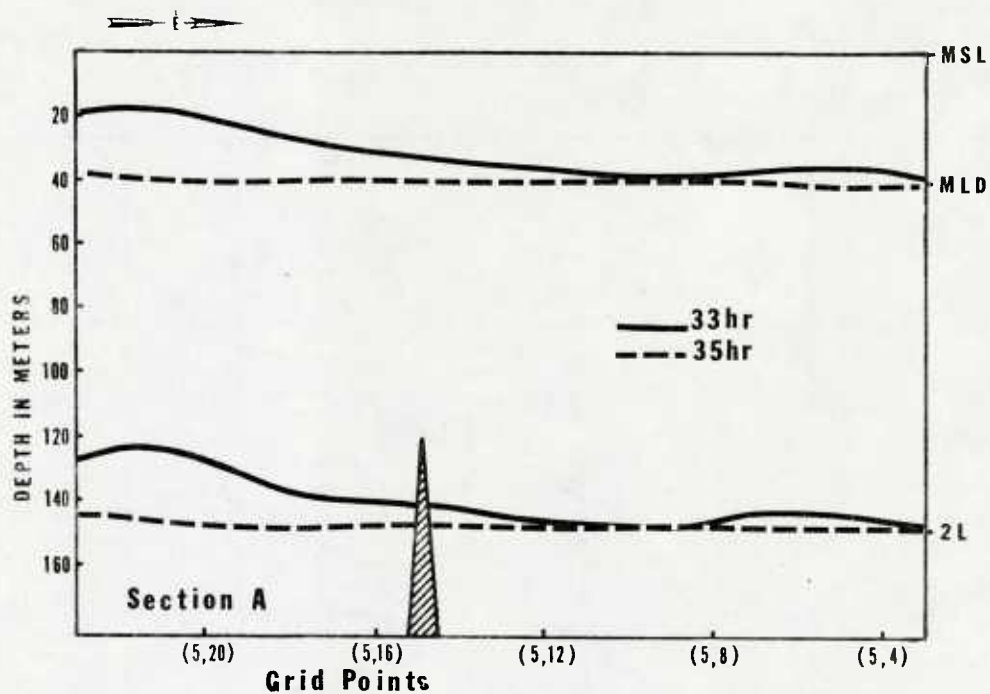
Figure 41. Depth of layer interfaces along sections A and B during and 2 hours after principal high water at Long Beach.

Figure 42. Sea level (cm) during principal low water at Long Beach.

- 64 -
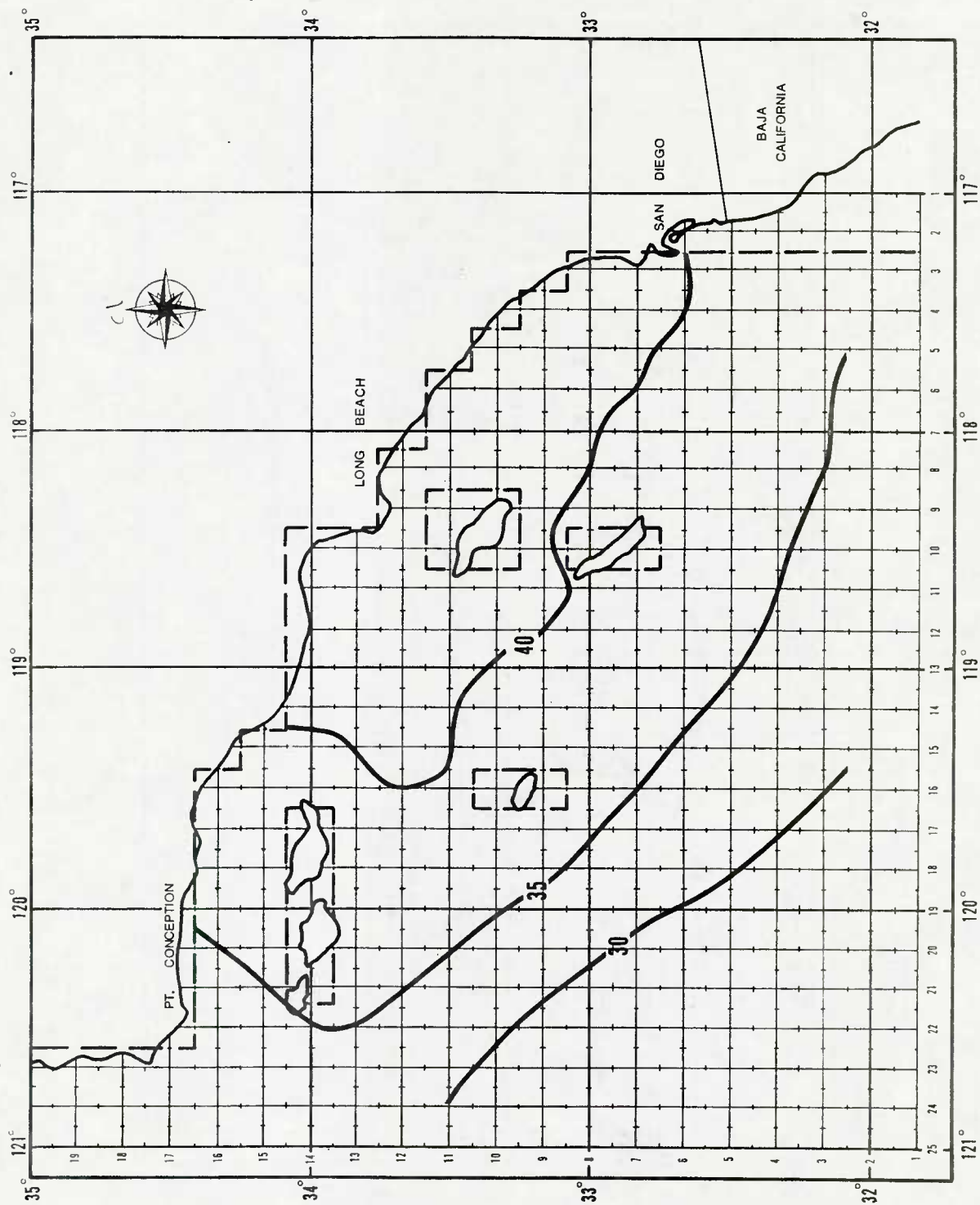
Figure 43. Sea level (cm) during secondary high water at Long Beach.

- 65 -
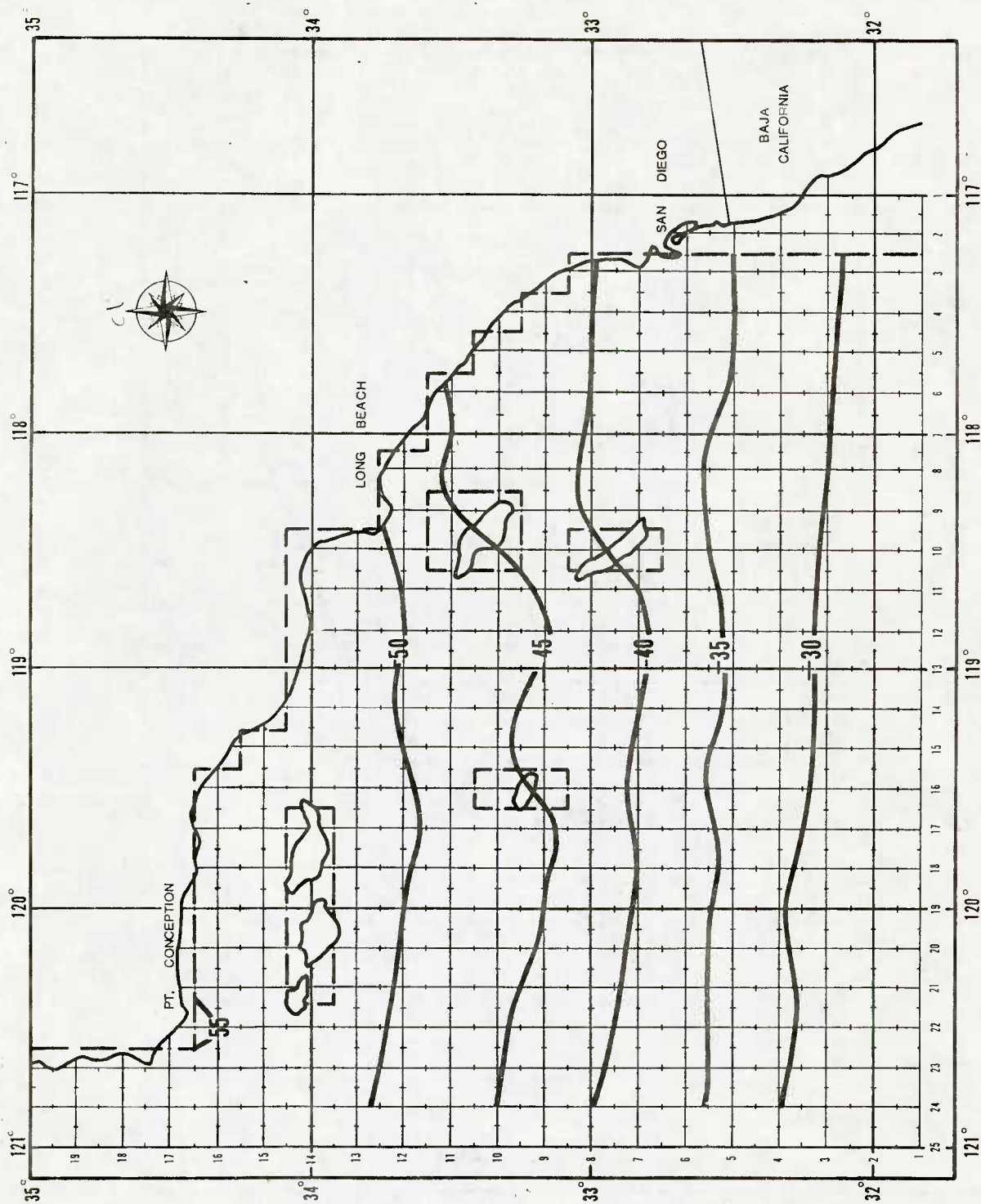
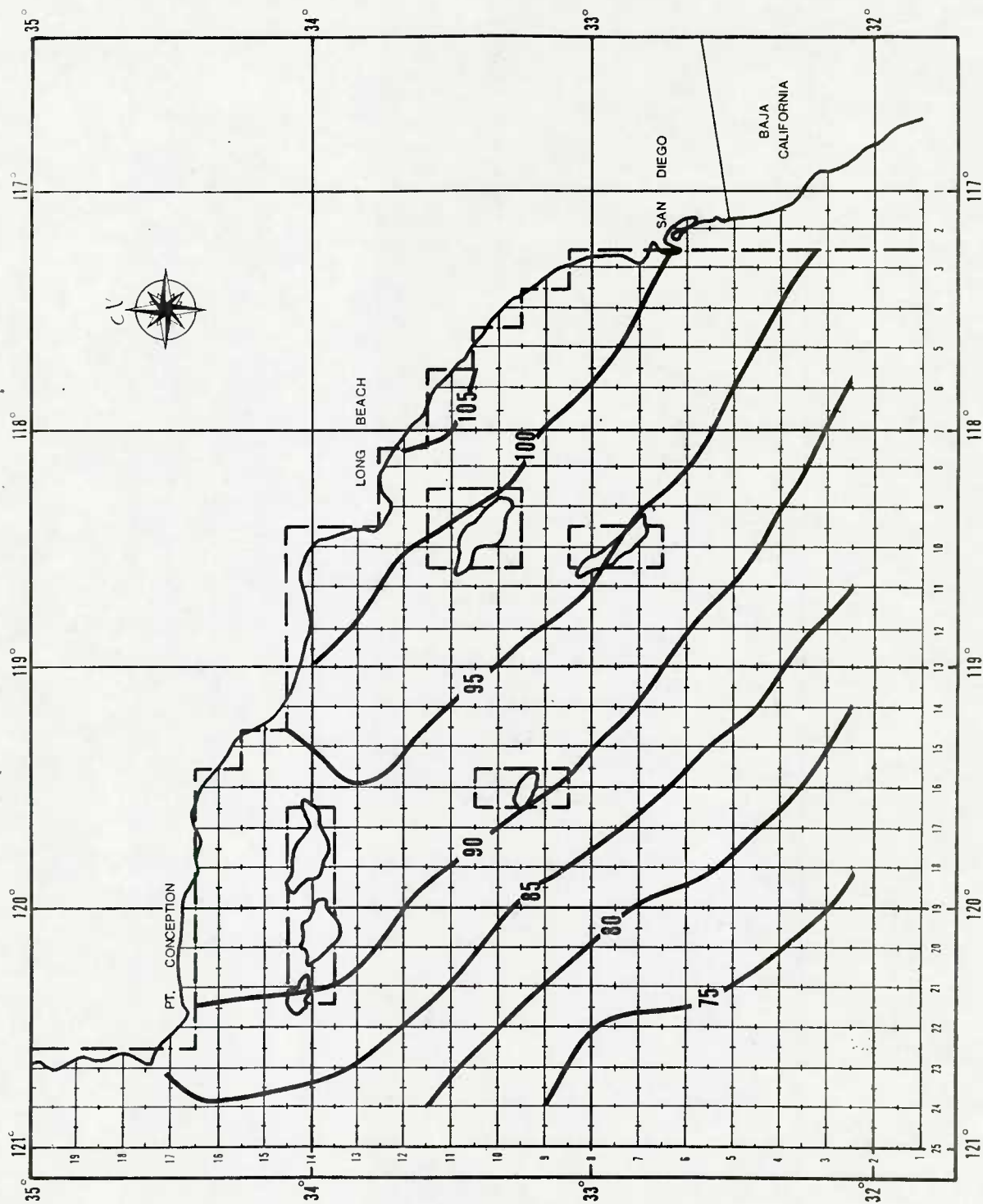Figure 44. Sea level (cm) during secondary low water at Long Beach.

- 66 -

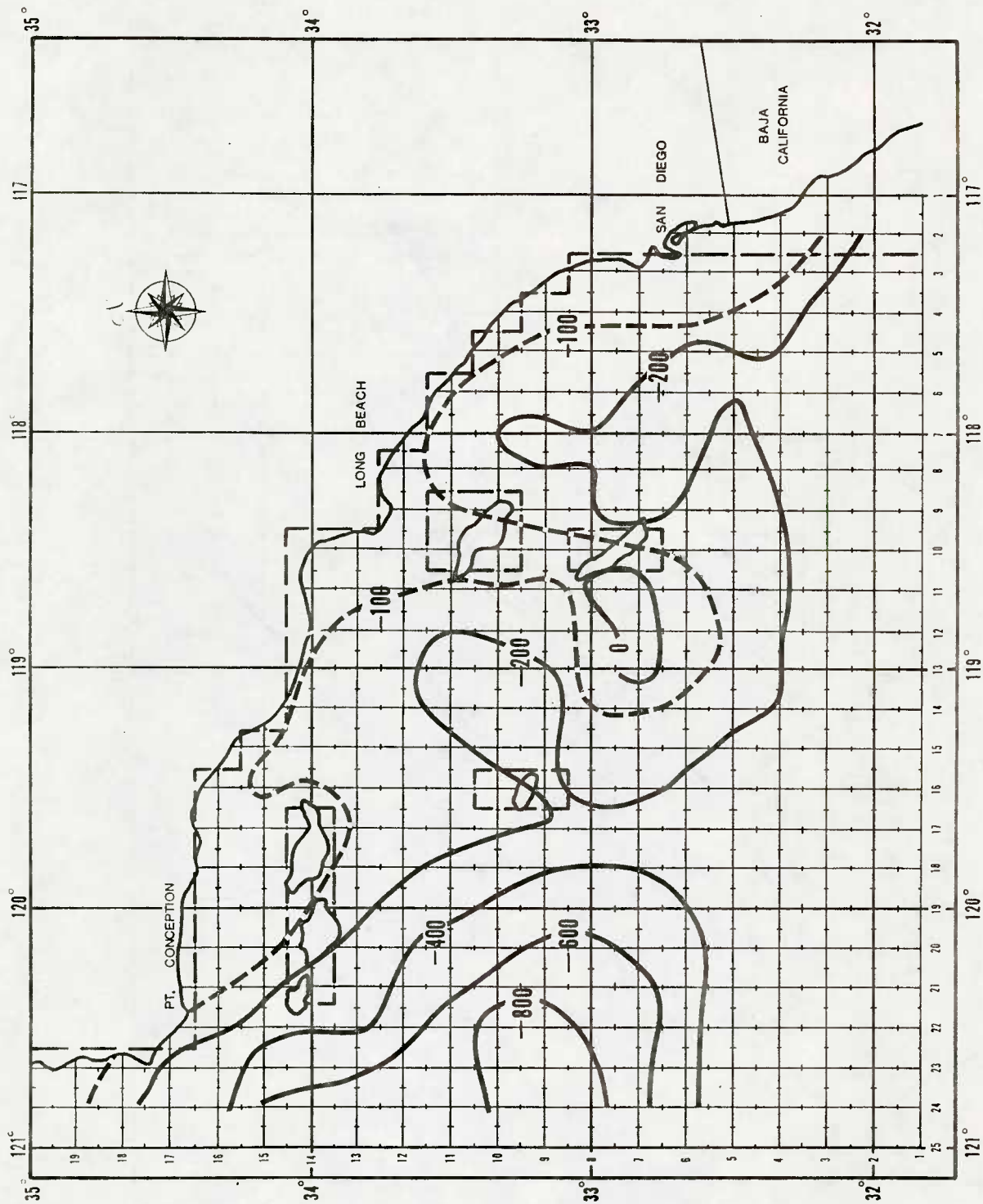Figure 45. Sea level (cm) during principal high water at Long Beach.

Figure 46. Deviation of lower boundary of the surface layer (MLD) from its
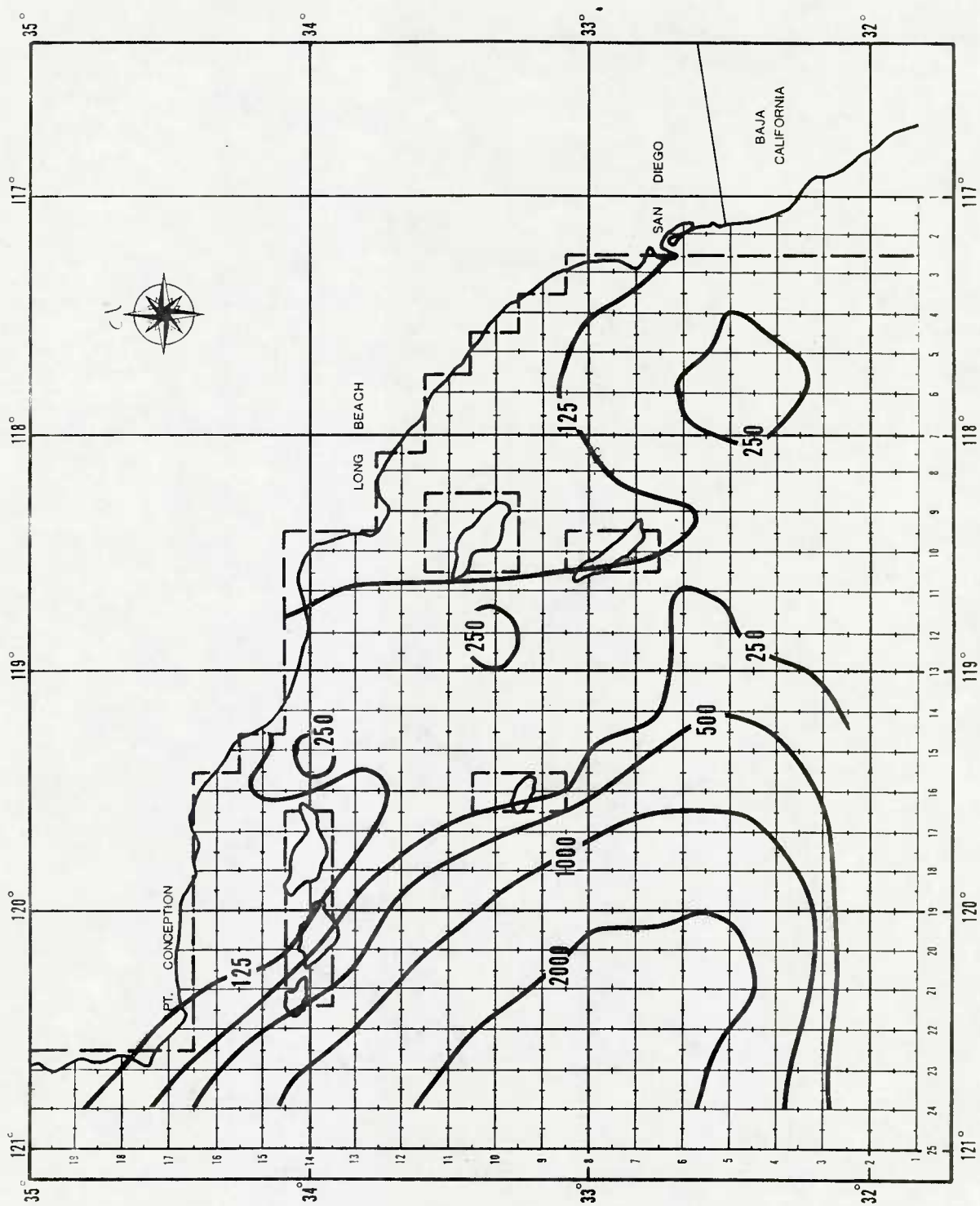mean value (cm) during principal low water at Long Beach.

Figure 47. Deviation of lower boundary of the surface layer (MLD) from its mean value (cm) during secondary high water at Long Beach.
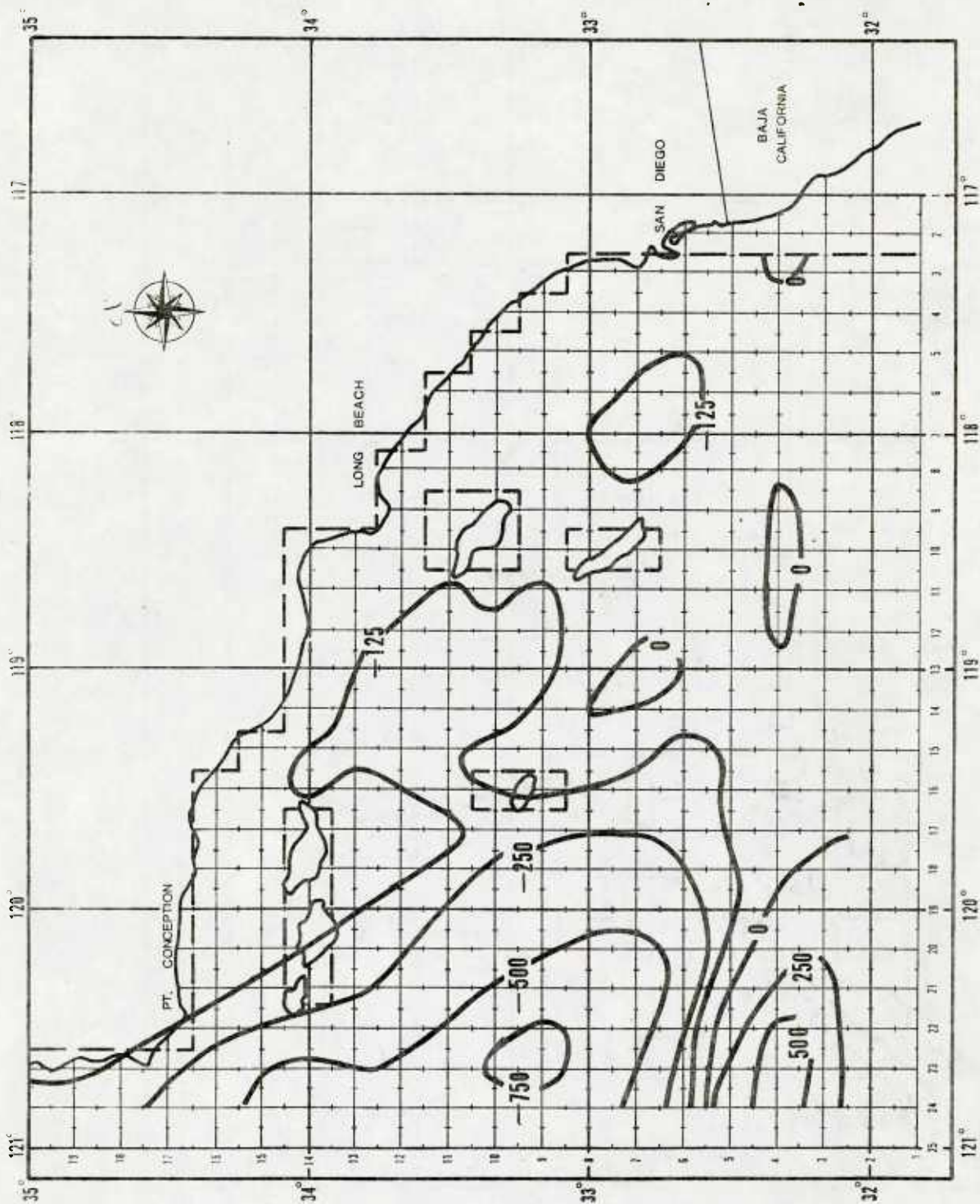
- 69 -

Figure 48. Deviation of lower boundary of the surface layer (MLD) from its mean value (cm) during secondary low water at Long Beach.
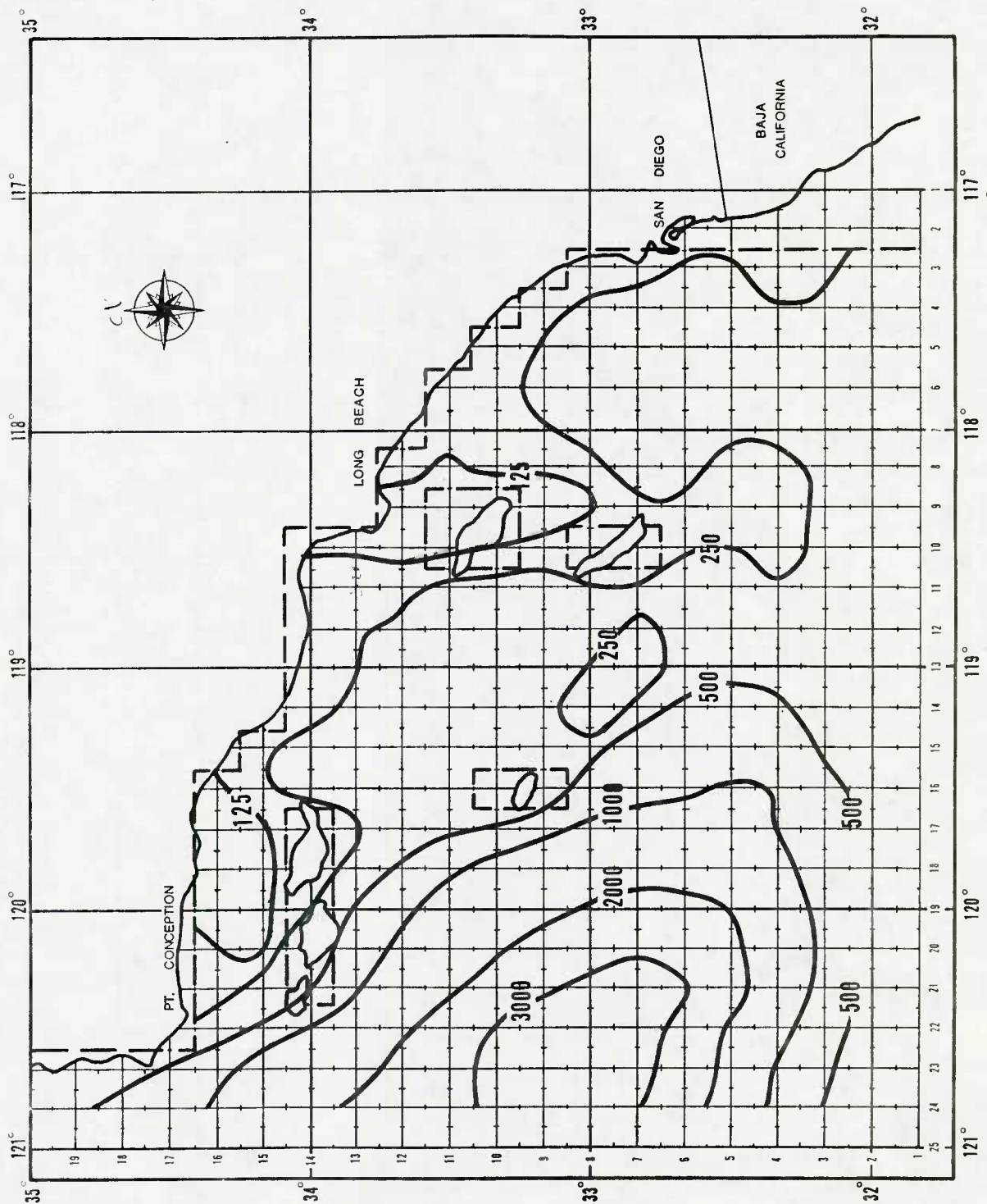
Figure 49. Deviation of lower boundary of the surface layer (MLD) from its mean value (cm) during principal high water at Long Beach.
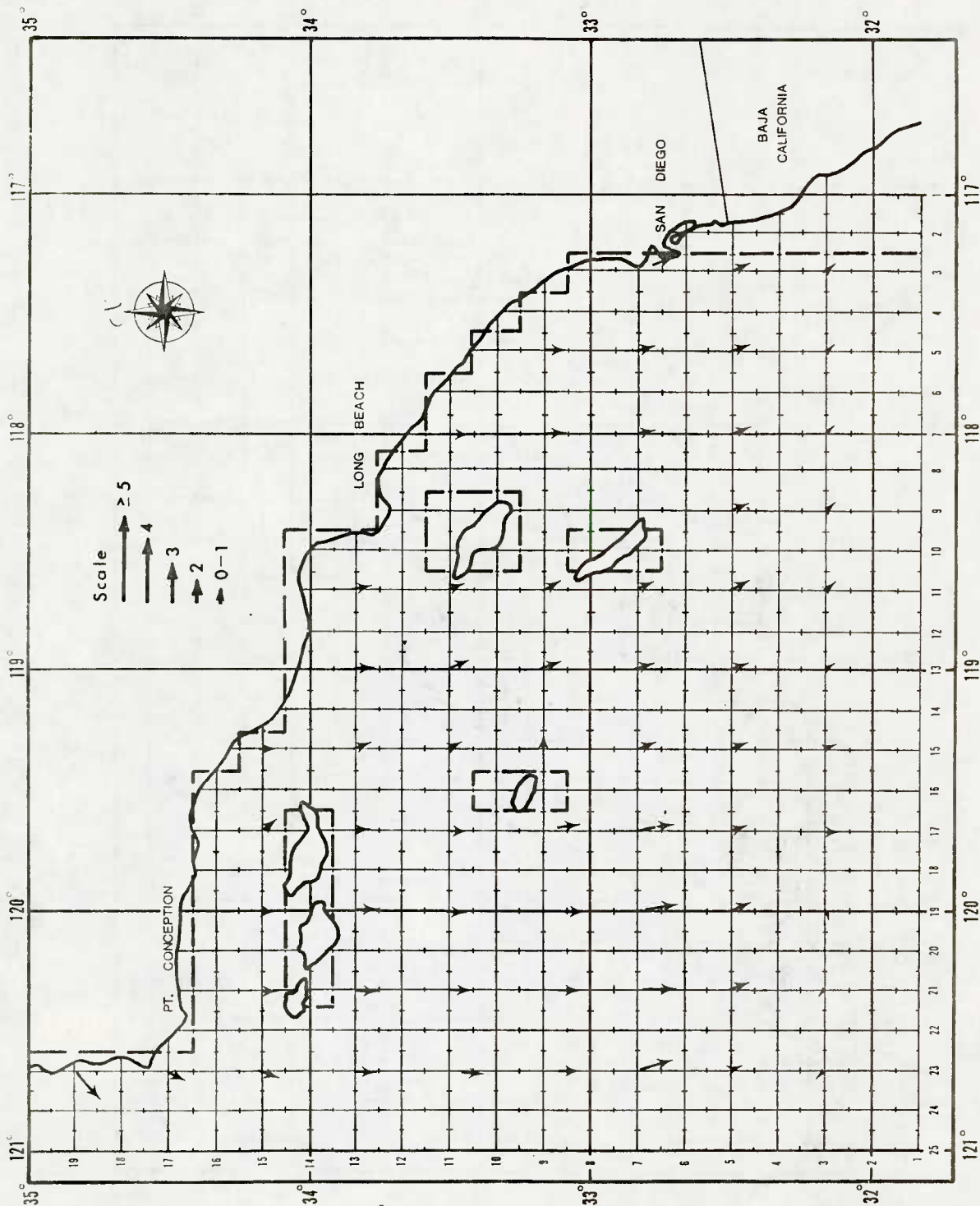
Figure 50. Rest currents after a full tidal cycle with wind from NNW, 8 m sec^{-1}.

U164516